Universidade de Brasília - UnB

Faculdade de Ciências e Tecnologias em Engenharia (FCTE)

Experimental Study of Blending Fuel Combustion Characteristics in a Hybrid Slab Burner Engine

Autor: Nicolle Augusta Moreira Lucena

Professor: Dr. Olexiy Shynkarenko

Brasília, DF

2025

Nicolle Augusta Moreira Lucena

Experimental Study of Blending Fuel Combustion Characteristics in a Hybrid Slab Burner Engine

Undergraduate thesis submitted to the undergraduate course in Aerospace Engineering of the Universidade de Brasilia, as partial requirement for obtaining the Bachelor's Degree in Aerospace Engineering

Universidade de Brasília - UnB

Faculdade de Ciências e Tecnologias em Engenharia (FCTE)

Orientador: Dr. Olexiy Shynkarenko

Brasília, DF

2025

Nicolle Augusta Moreira Lucena
Experimental Study of Blending Fuel Combustion Characteristics in a Hybrid Slab Burner Engine/ Nicolle Augusta Moreira Lucena. – Brasília, DF, 2025-
84 p. : il. (algumas color.) ; 30 cm.

Orientador: Dr. Olexiy Shynkarenko

Undergraduate Thesis –
Universidade de Brasília - UnB
Faculdade de Ciências e Tecnologias em Engenharia (FCTE)
, 2025.

1. . 2. . I. Dr. Olexiy Shynkarenko. II. Universidade de Brasília. III. Faculdade de Ciências e Tecnologias em Engenharia (FCTE). IV. Experimental Study of Blending Fuel Combustion Characteristics in a Hybrid Slab Burner Engine

CDU 02:141:005.6

Nicolle Augusta Moreira Lucena

Experimental Study of Blending Fuel Combustion Characteristics in a Hybrid Slab Burner Engine

Undergraduate thesis submitted to the undergraduate course in Aerospace Engineering of the Universidade de Brasilia, as partial requirement for obtaining the Bachelor's Degree in Aerospace Engineering

Trabalho aprovado. Brasília, DF, :

Dr. Olexiy Shynkarenko
Orientador

Prof. Dr. Artur Elias de Morais Bertoldi
Convidado 1

Prof. Dr. Lui Txai Calvoso Habl
Convidado 2

Brasília, DF
2025

Abstract

This work experimentally investigated the regression rate behavior of paraffin-based hybrid rocket fuels containing different concentrations of low-density polyethylene (LDPE), using a slab burner configuration. Twelve samples, four of each composition (PR100, PR95PE05, and PR90PE10), were tested under varying oxidizer mass fluxes. The regression rates were calculated by separately quantifying the liquid film contribution and consistently exceeded those reported in the literature, even under similar operating conditions. While increasing LDPE concentration led to lower total regression rates, it also reduced liquid film formation, suggesting a trade-off between regression rate and combustion efficiency. These results confirmed the influence of viscosity and melt-layer behavior on entrainment mechanisms and reinforced the importance of optimizing fuel formulations based on application-specific goals.

Key-words: hybrid rocket propulsion. paraffin-based fuels. LDPE. regression rate. combustion efficiency. slab burner.

Lista de ilustrações

Lista de tabelas

Lista de abreviaturas e siglas

CEA	Chemical Equilibrium with Applications
CPL	Chemical Propulsion Laboratory
CPU	Central Processing Unit
DAQ	Data Acquisition System
EVA	Ethylene Vinyl Acetate
FAPDF	Fundação de Apoio à Pesquisa do Distrito Federal
GOX	Gaseous Oxygen
HDPE	High-Density Polyethylene
HRE	Hybrid Rocket Engine
HRM	Hybrid Rocket Motor
HTPB	Hydroxyl-terminated Polybutadiene
KAU	Korea Aerospace University
LDPE	Low-Density Polyethylene
MOUETTE	Moteur OptiqUe pour ÉTudier et Tester Ergols
NI	National Instruments
ONERA	French Aerospace Lab
O/F	Oxidizer-to-Fuel ratio
PE	Polyethylene
PR100	Pure paraffin wax
PR90PE10	Blended fuel of 90 wt % pure paraffin wax and 10 wt % PE
PR95PE05	Blended fuel of 95 wt % pure paraffin wax and 5 wt % PE
RMA	Royal Military Academy of Belgium
TU	Tokai University
ULB	Université Libre de Bruxelles
UnB	Universidade de Brasília

Resumo

Este trabalho investigou experimentalmente o comportamento da taxa de regressão de combustíveis de foguete híbridos à base de parafina contendo diferentes concentrações de polietileno de baixa densidade (LDPE), utilizando um slab burner. Doze amostras, quatro de cada composição (PR100, PR95PE05 e PR90PE10), foram testadas sob diferentes fluxos de massa de oxidante. As taxas de regressão foram calculadas quantificando-se a contribuição do filme líquido e excederam consistentemente os valores apresentados na literatura, mesmo em condições operacionais semelhantes. Embora o aumento na concentração de LDPE tenha levado a menores taxas de regressão total, também reduziu a formação de filme líquido, sugerindo uma compensação entre a taxa de regressão e a eficiência de combustão. Esses resultados confirmaram a influência da viscosidade e do comportamento da camada liquida de parafina nos mecanismos de arraste (entrainment) reforçando a importância da otimização das formulações de combustível com base nos objetivos específicos de aplicação.

Key-words: propulsão de foguetes híbridos. combustíveis à base de parafina. LDPE. taxa de regressão. eficiência de combustão. slab burner.

Sumário

List of Symbols

A_b	Burning area
A_e	Exit area
A_o	Orifice area
A_{port}	Port area
A_t	Exhaust nozzle throat area
A_w	Wet area
C_d	Discharge coefficient
F	Thrust
G_o	Oxidizer mass flux
G_{tot}, G	Total free-stream propellant mass flux
I_s	Specific impulse
P_a	Ambient pressure
P_c	Chamber pressure
P_d	Dynamic pressure in the port
P_e	Gas exit pressure
P_t	Tank pressure
R	Gas constant
T	Temperature
V	Volume
a	Regression rate coefficient
a_{ent}	Absorption coefficient
β	Fuel mass flux coefficient
c^*_{act}	Experimental characteristic velocity
c^*_{theo}	Theoretical characteristic velocity
Δm_f	Fuel mass difference
g_0	Standard sea-level gravitational acceleration
g_c	Conversion factor
γ	Specific heat ratio
h	Melt layer thickness
η_c	Combustion efficiency
m_c	Mass of collected fuel

$\dot{m}$	Total mass flow rate
$\dot{m}_{ent}$	Entrainment component of mass flux from the fuel surface
$\dot{m}_f$	Fuel mass flow rate
$\dot{m}_{lf}$	Liquid film mass flow rate
$\dot{m}_{ox}$	Oxidizer mass flow rate
$\dot{m}_{v+e}$	Vaporization and entrainment mass flow rate
n	Oxidizer mass flux exponent
$\overline{\dot{r}}$	Time–space-averaged fuel regression rate
μ	Combustion gas viscosity
μ_l	Liquid fuel viscosity
t_b	Burning time
u_e	Flow velocity at exit
x	Axial distance from the leading edge of the fuel grain
ρ	Specific mass
ρ_f	Fuel grain density
σ	Surface tension
$\dot{r}$	Fuel regression rate
$\dot{r}_{ent}$	Entrainment regression rate
$\dot{r}_{lf}$	Liquid film regression rate
$\dot{r}_{tot}$	Total regression rate
$\dot{r}_{v+e}$	Regression rate of the vaporization and entrainment

1 Introduction

1.1 Background and Motivation

The development of space technologies is a key element for all nations, playing a crucial role in various sectors such as space exploration, satellite communications, national defense and security, as well as generating economic benefits from the advancement of such technologies. The space business industry not only represents a new source of economic growth, but also has the potential to positively impact society as a whole, as the technologies developed in this field can be applied across a wide range of distinct sectors.

Rocket propulsion systems may be classified by the method of producing thrust. In chemical rocket propulsion (CRP) the energy from the combustion reaction of chemical propellants, usually a fuel and an oxidizer, in a high-pressure chamber goes into heating reaction product gases to high temperatures and these gases are subsequently expanded in a supersonic nozzle and accelerated to high velocities. In this system, the internal energy of the propellant is converted into exhaust kinetic energy and thrust is also produced by the pressure on surfaces exposed to the exhaust gases (SUTTON; BIBLARZ, 2017).

Among the various categories of chemical propulsion, hybrid rocket propulsion systems represent a distinctive configuration in which the fuel and oxidizer are stored in different physical states, typically a solid fuel and a liquid or gaseous oxidizer. This configuration has features of both solid and liquid propulsion systems, offering simplicity, storability, and controllability. Hybrid rockets can be throttled, stopped, and restarted during flight, are more compact than liquids rockets, and typically achieve higher specific impulse than solids rockets, resulting in greater flexibility and flight control throughout the rocket's trajectory (JENS; CANTWELL; HUBBARD, 2016). Due to these advantages, hybrid propulsion has attracted growing interest for research, educational, and small satellite launch vehicle applications. New hybrid rocket motors (HRMs) are under development not only for orbital launch vehicles but also for university rockets and experimental propulsion systems, reflecting the versatility and safety of this propulsion system (KARAKAS et al., 2020).

Various launch vehicles are currently being developed, particularly those powered by hybrid propulsion using paraffin-based fuels. Figure 1 illustrates two successful commercial launches of hybrid rockets. On the left is Spaceship Two, developed by Virgin Galactic, which had its first successful launch in 2004. On the right is the Hanbit rocket, developed by Innospace and successfully launched in Alcântara, Brazil, in 2023. These examples demonstrate the viability of hybrid propulsion for space missions and contri-

bute to increasing its reliability and applicability. Although hybrid rockets are generally considered safe and cost-effective, challenges such as boundary-layer combustion and low fuel regression rates must be addressed to optimize its performance (OISHI; TAMARI; SAKURAI, 2023).

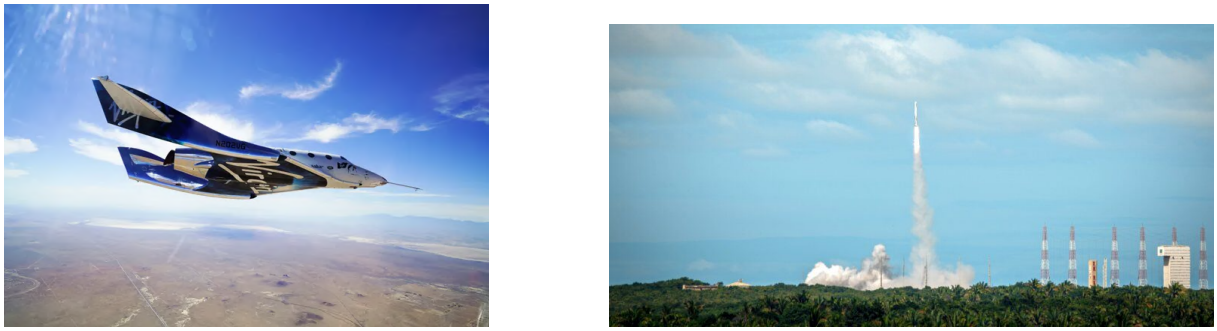

Figura 1 – Successful hybrid rocket launches (WRITERS, 2013; MUNDOGEO, 2023).

The most important disadvantage of conventional hybrid rocket motors is the low fuel regression rate, which limits the achievable thrust. Even so, this issue can be mitigated through the use of paraffin-based fuels, which present three to five times higher regression rates than common polymeric fuels like hydroxyl-terminated polybutadiene (HTPB). This improvement is attributed to the liquefying behavior of paraffin under combustion conditions, which promotes enhanced mass transfer and turbulent entrainment (KARABEYOGLU; ALTMAN; CANTWELL, 2002; KARAKAS et al., 2020).

The droplet entrainment theory, proposed by (KARABEYOGLU; ALTMAN; CANTWELL, 2002), explains this enhanced performance as the result of shear-induced droplet formation on a liquefied fuel layer with low viscosity and surface tension. This mechanism significantly boosts the mass transfer rate in addition to surface vaporization.

In subsequent research by (LEE et al., 2023), a significant amount of liquid paraffin mass accumulation was observed at the bottom of the post-combustion chamber. Based on these findings, a third mechanism of mass transfer was proposed: the formation of a flowing liquid film on the surface of the fuel, which may further enhance the overall regression rate. Understanding the individual contribution of these three mechanisms (vaporization, droplet entrainment, and liquid film flow) is crucial for improving combustion models and optimizing hybrid rocket motor design.

1.2 Objectives and Expected Results

The objective of this research is to study three types of fuel regression rates: total ($\dot{r}_{tot}$), due to liquid film ($\dot{r}_{lf}$), and vaporization and entrainment ($\dot{r}_{v+e}$), of paraffin-based fuels blended with low-density polyethylene (LDPE) in different concentrations (0%, 5%,

and 10%) using gaseous oxygen as oxidizer and a two-dimensional slab burner. Also, combustion efficiency will be evaluated, and how different percentages of additive mixtures and fuel viscosity influences both regression rates and overall combustion performance.

General Objectives

1. Characterization of Fuel Samples
    - Analyze the properties of fuel blends in combustion tests.

The expected results will allow for a direct comparison with those presented in Figure 2, which illustrates the regression rates as a function of total propellant mass flux (G_{tot}) for the PR100, PR95PE05 and PR90PE10 fuels, performed at Korea Aerospace University (KAU).

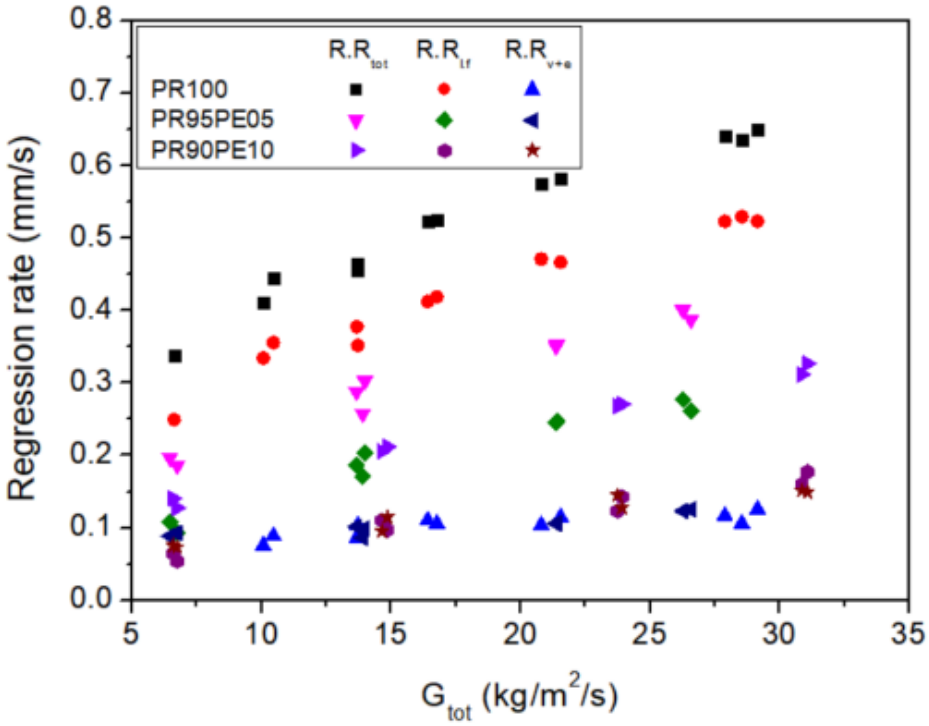

Figura 2 – Regression rates for paraffin-based fuels (LEE et al., 2023).

The ultimate goal is to experimentally study the regression rate and characteristics of paraffin-based fuels and evaluate their efficiency in a slab burner engine, providing valuable insight regarding the practicality of using this fuel mixture in actual full-scale engines. Other projects developed by the Chemical Propulsion Laboratory (CPL) of Universidade de Brasília (UnB), such as the SARA V2 and SARA V3, may directly benefit from the results obtained in the slab burner. Since this configuration allows for the analysis of regression rate without the need to manufacture full-scale grains, it can serve as a preliminary fuel screening tool. Only after promising formulations are validated in this

simplified configuration will they be selected for more comprehensive testing in larger hybrid rocket engines.

In short, the specific objectives are:

Specific Objectives

1. Study of Regression Rates
    - Investigate the regression rates of three types of paraffin-LDPE-based fuel blend concentrations, including:
        - Total regression rate ($\dot{r}_{tot}$)
        - Liquid film regression rate ($\dot{r}_{lf}$)
        - Regression due to vaporization and droplet entrainment ($\dot{r}_{v+e}$)
2. Combustion Efficiency Evaluation
    - Evaluate combustion efficiency and its relationship with different additive mixtures.
3. Influence of Viscosity
    - Assess how the viscosity of the fuel influences regression rates and overall combustion performance.
4. Comparison with Previous Data
    - Allow for a direct comparison of the results obtained with those presented in existing literature.

This study is of significant importance for advancing hybrid propulsion methodologies at the Chemical Propulsion Laboratory (CPL), as it provides empirical data that can support the development of more efficient propulsion technologies. By understanding the combustion behavior of paraffin-based blends, this research may help optimize fuel performance and improve the overall efficiency of hybrid propulsion systems. Additionally, the implementation of combustion tests using the slab burner strengthens the laboratory's experimental infrastructure and supports ongoing and future researches.

2 Literature Review

2.1 Principles of Hybrid Combustion and Hybrid Rocket Engines (HRE)

In general terms, propulsion is the act of changing the motion of a body with respect to an inertial reference frame. Propulsion systems provide forces that either move bodies initially at rest or change their velocity or that overcome retarding forces when bodies are propelled through a viscous medium. Among the various types of propulsion, rocket propulsion is a class of jet propulsion that produces thrust by ejecting matter, called the working fluid or propellant, stored entirely in the flying vehicle (SUTTON; BIBLARZ, 2017).

Propulsion has historically been employed as a means of both defense and attack, particularly throughout the 18th and 19th centuries. However, one of the earliest documented uses of propulsion dates back to ancient China, where solid propellants based on gunpowder were utilized in the development of so-called "fire arrows."These early devices, illustrated in Figure 3, are considered precursors to modern rocket technology. Functioning on similar principles to contemporary fireworks, these fire arrows demonstrated the fundamental concept of using controlled combustion to generate thrust and project objects over distance.

Figura 3 – Chinese fire arrow. Adapted from (NASA, Unknown year)

As described by (SUTTON; BIBLARZ, 2017), rocket propulsion bipropellant concepts in which one component propellant is stored in the liquid phase, and the other as a solid is called "hybrid propulsion systems"or "hybrid rocket engines". Specifically for the hybrid rocket motors, which is a form of chemical propulsion system, the fuel and oxidizer are in two different states: typically, the fuel is solid, and the oxidizer is a gas/liquid, providing a highly dense fuel source similar to a bi-propellant solid motor but with the

throttle control of a liquid motor (KARABEYOGLU, 1998).

In hybrid propulsion rockets, the fuel is contained within the combustion chamber as a cylindrical grain with one or more hollow channels (ports) along its axis, and the oxidizer is delivered to the combustion chamber through a single fluid feed system, controlled by a main run valve. A schematic of a hybrid rocket is shown in Figure 4, where the main systems for its operation are presented.

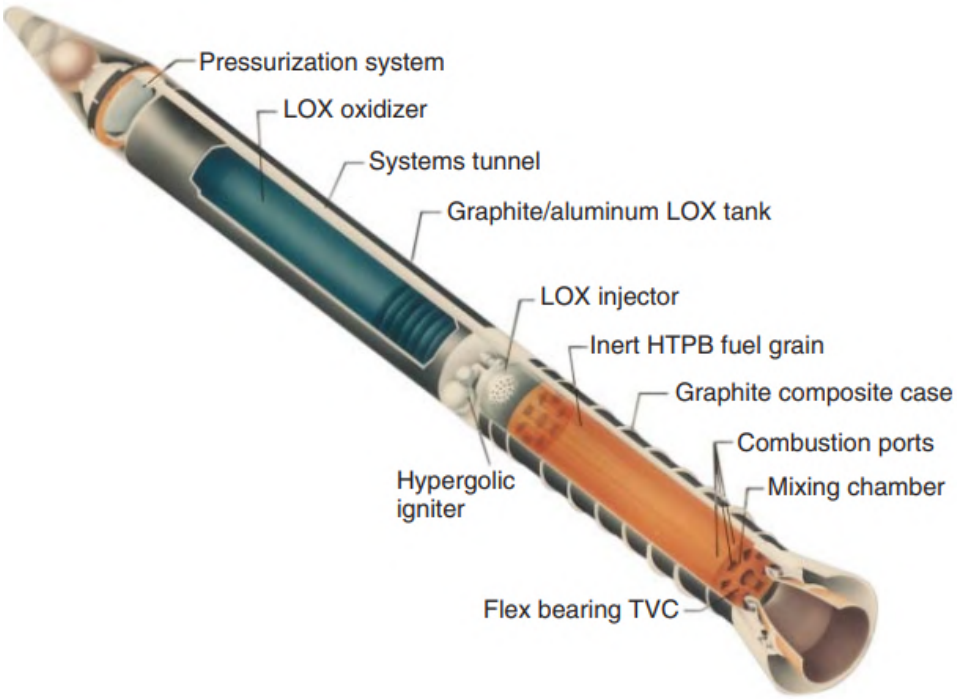

Figura 4 – Description of a hybrid rocket preliminary concept having an inert solid fuel grain and pressurized liquid oxygen feed system. Adapted from (SUTTON; BIBLARZ, 2017).

The study of thermochemistry is essential to understanding and designing rocket propulsion systems. This field governs the selection of propellants, the combination of fuel and oxidizer, which directly influences the combustion chamber temperature and the molecular masses of the resulting products. These properties affect key performance parameters such as exhaust gas velocity and specific impulse (HUMBLE; LARSON, 2007).

Combustion, defined as a rapid oxidation process that releases heat (and often light), requires the fuel to reach its ignition temperature and to be mixed with the oxidizer in appropriate proportions (TURNS, 2011). Simply placing the fuel in contact with the oxidizer is not sufficient: ignition only occurs if these thermodynamic and stoichiometric conditions are satisfied. In hybrid propulsion, where fuel is solid and oxidizer is typically a liquid or gas, this interaction occurs at the fuel surface in a turbulent boundary layer, making the thermochemical behavior even more complex.

The combustion process can be classified as complete or incomplete. Complete

combustion occurs when sufficient oxidizer is available, resulting in fully oxidized products like carbon dioxide and water. Incomplete combustion, by contrast, results from limited oxygen or poor mixing, producing pollutants such as carbon monoxide or unburned hydrocarbons. Even with excess oxidizer, real combustion in rocket chambers may remain incomplete due to short residence times or diffusion limitations (ÇENGEL, 2013).

In theory, the ideal case is stoichiometric combustion, where the exact amount of oxidizer reacts with the fuel, yielding no leftover reactants. The heat released during this reaction is calculated through the enthalpy difference between products and reactants:

$$Q_{reaction} = \Delta H = H_{products} - H_{reactants} \tag{2.1}$$

This energy release, known as the enthalpy of combustion (h_c), can be used to estimate the thermal load in the chamber and is closely linked to the fuel's heating value. The enthalpy of formation (h_f) of individual species is also used in calculating the net enthalpy of the reaction. These parameters are fundamental for determining the thermal efficiency of the propulsion system and for sizing insulation, tanks, and cooling systems.

A complete understanding of combustion chemistry not only allows for accurate performance prediction but also supports key design decisions such as material selection and thermal management strategies. The thermochemical behavior in hybrid rockets, where fuel undergoes pyrolysis and vaporization before reacting, is particularly important. This is visually represented in Figure 5, which shows the schematic of the combustion chamber of a HRE.

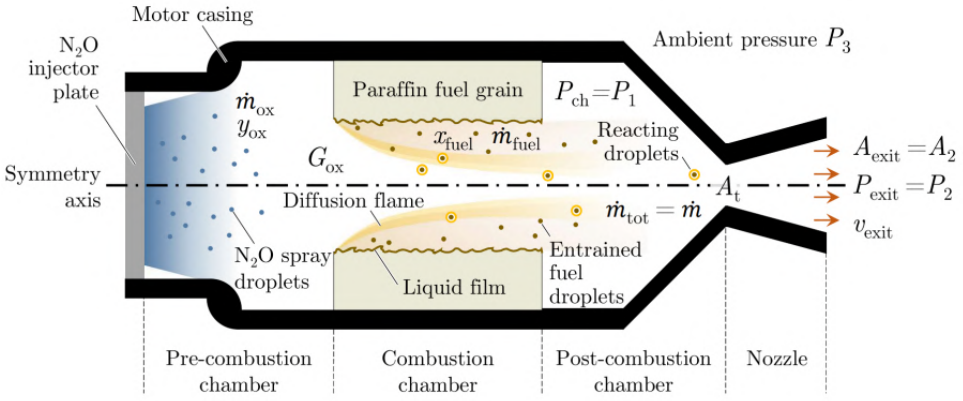

Figura 5 – Schematic of the combustion chamber of a hybrid rocket engine (DEQUICK, 2022).

An igniter vaporizes a portion of the fuel to initiate combustion, which occurs within a turbulent boundary layer[1] through diffusive mixing between the oxidizer flowing

[1] The boundary layer is the region of the flow near a surface that has reduced flow velocity due to viscous shear forces between the flow and the surface. The velocity is zero at the surface and must increase to a maximum at the boundary layer edge (HUMBLE; HENRY; LARSON, 1995).

through the port and the fuel melting, pyrolyzing and evaporating from the solid surface. The oxidizer enters the flame zone from the port free-stream core by diffusion, while the fuel enters the boundary layer due to vaporization at the wall surface. The combustion zone is established when an approximate stoichiometric mixture ratio has been achieved (HUMBLE; HENRY; LARSON, 1995). This model is illustrated in Figure 6.

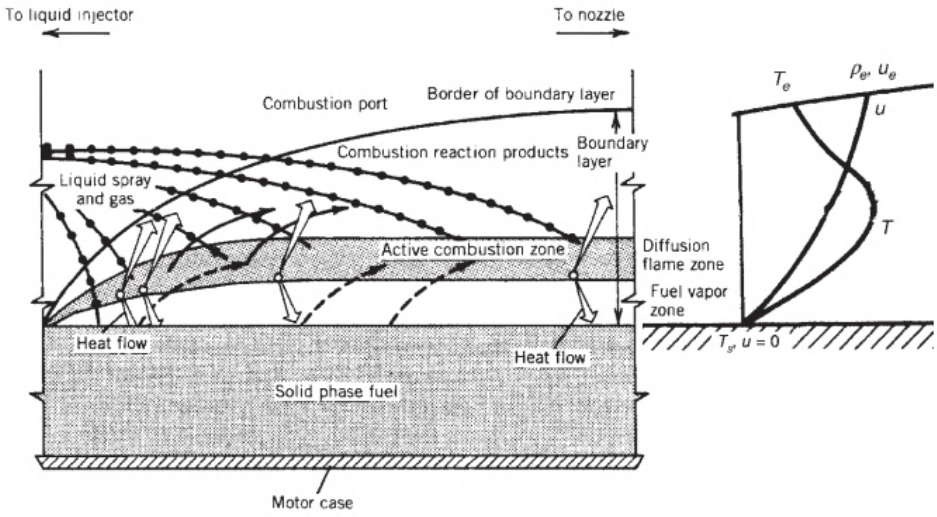

Figura 6 – Simplified model of a diffusion-controlled hybrid combustion process, illustrating a flame zone embedded within the fuel boundary layer (SUTTON; BIBLARZ, 2017).

As described in Figure 6, the primary combustion region is confined to a narrow flame zone within the boundary layer that forms and grows over the fuel grain surface. Heat is transferred to the grain surface through convection and radiation, causing the fuel to vaporize. The vaporized fuel flows from the surface toward the flame region, while the oxidizer convects from the free stream to the flame zone by turbulent diffusion. Due to the empirical nature of hybrid propulsion research, motor characteristics are highly dependent on the propellant system, as well as the scale and configuration of the combustion chamber (SUTTON; BIBLARZ, 2017).

With nonmetallized fuel grains, at the pressures and flux levels of interest for propulsion applications, heat transfer by convection is considered to be much larger than that transferred by gas-phase radiation or radiation from soot particles in the flow. As a result, the basic characteristics of fuel grain regression may be explored via analyses of convective heat transfer in a turbulent boundary layer (SUTTON; BIBLARZ, 2017).

Unlike solid rocket motors, the fuel grain in the classical hybrid configuration contains no oxidizer, which means that combustion occurs only in the gaseous phase, and the rate at which the solid fuel is converted to gaseous vapor is a very important parameter, known as the regression rate (KUO; CHIAVERINI, 2007). Since the solid fuel must vaporize before combustion, the regression rate is inherently tied to the interaction between

combustion port fluid dynamics and heat transfer to the fuel grain surface (SUTTON; BIBLARZ, 2017).

The fuel regression rate ($\dot{r}$) is the rate at which the solid is consumed or eroded by the combustion process, as described above, and is an important parameter because it affects the performance and stability of the engine, in addition to directly defining the thrust and geometry of the motor (ZILLIAC; KARABEYOGLU, 2006). Thus, Equation 2.2 can be used to describe the fuel regression rate (SUTTON; BIBLARZ, 2017).

$$\dot{r} = 0.036 \frac{G^{0.8}}{\rho_f} \left(\frac{\mu}{x}\right)^{0.2} \beta^{0.23} \tag{2.2}$$

Equation 2.2 indicates that hybrid fuel regression rates in a non-radiative regime are strongly dependent on the total free-stream propellant mass flux and rather weakly dependent on both axial location (x) and fuel blowing characteristics (β) (SUTTON; BIBLARZ, 2017). It is also important to note that the G parameter represents the total mass flux, which includes both the injected oxidizer and the fuel vaporized from the surface of the fuel wall.

This first approach to the regression rate is commonly known as classical theory, which only considers the vaporization portion of the fuel grain. However, over the years, with the advancement of studies in the area, new theories have been proposed to better explain and predict the combustion behavior of liquefying hybrid propellants, such as paraffin, which form a liquid layer on the burning surface of the grain.

When the paraffin-based fuel is heated, a thin, melted liquid layer with lower viscosity forms on the surface of the solid fuel. This is accompanied by an unstable wave motion created by the incoming oxidizer. Significant droplets of liquid fuel produced at the tips of the wavelets are drawn into the gas stream, where this entrained mass of liquid droplets increases the regression rate.

In addition to classical gasification, the modern regression rate model developed for these liquefying propellants is based on a mass transfer mechanism of those liquid droplets from the melt layer (KARABEYOGLU; ALTMAN; CANTWELL, 2002). This behavior can be seen in Figure 7, which demonstrates a schematic of the oxidizer flux over the grain, showing that droplets are formed and dragged during the paraffin combustion process, contributing to the total mass flow rate of the fuel.

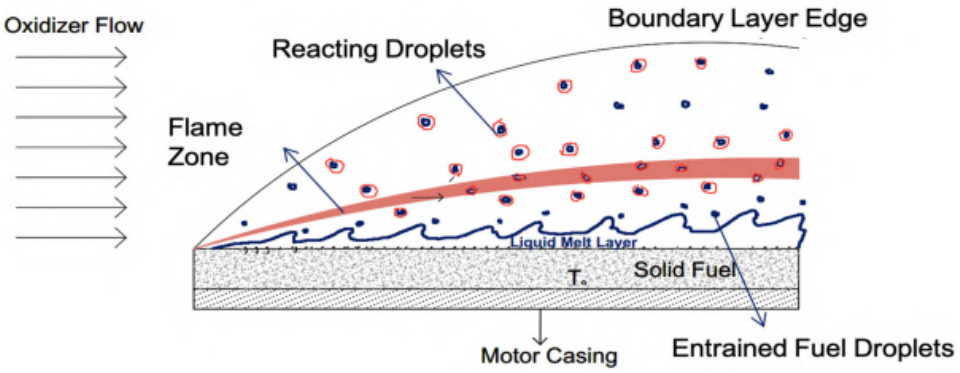

Figura 7 – The combustion process of paraffin wax-based fuels in hybrid rockets (MAHOTTAMANANDA et al., 2022).

The mass flow rate relationship for these droplet entrainments was suggested by Karabeyoglu et al. [parte1], described in Equation 2.3, including the dynamic pressure, the thickness of the melt layer, the surface tension and the viscosity of the melt layer. Also, the entrainment regression rate can be written in terms of the mass flux in the port and the total regression rate, using Equation 2.4. Lastly, Equation 2.5 calculates the overall regression rate for different types of solid fuel, using experimental data and variables according to each fuel used.

$$\dot{m}_{\text{ent}} \propto \frac{P_d^{\alpha} h^{\beta}}{\mu_l^{\gamma} \sigma^{\pi}} \tag{2.3}$$

$$\dot{r}_{\text{ent}} = a_{\text{ent}} \left(G^{2\alpha} / \dot{r}^{\beta} \right) \tag{2.4}$$

$$\bar{\dot{r}} = a \bar{G}_o^n \tag{2.5}$$

Table 3 presents a selection of coefficient values associated with various fuels, intended for application in Equation 2.5, and delineates the comparative rate of escalation of the regression rate for each fuel to polyethylene (PE).

Tabela 3 – Comparison of regression rate correlations between several liquefying and non-liquefying fuels (KIM et al., 2015).

Fuel type	**Regression rate coefficient,** a	**Oxidizer mass flux exponent,** n	**Rate of increase relative to PE**
PR100	0.410	0.37	6.4
SP-1a	0.117	0.62	5.7
PR95PE05	0.234	0.39	3.9
PR90PE10	0.120	0.49	3.0
HTPB	0.072	0.50	2.0
PE	0.026	0.58	1.0

With Table 4 serving as a reference point, it is possible to derive several overarching conclusions regarding hybrid propulsion systems. Because propellant is stored in different states and phases, explosive mixtures that can occur in liquid or solid rockets are impossible. Also, the fuel is classified as inert, contributing to much more simplified storage and handling.

Tabela 4 – Advantages and Disadvantages of Hybrid Propulsion Systems. Adapted from (SUTTON; BIBLARZ, 2017).

Advantages	**Disadvantages**
More safety and strength than conventional chemical propulsion systems.	Mixture ratio and specific impulse may vary during steady flow operation and throttling.
Start-stop–restart capabilities.	Requires relatively complicated solid geometries, leading to significant fuel residues that reduce mass fraction and vary unpredictably.
Relative simplicity compared to liquid propulsion systems, potentially reducing overall system cost.	Prone to large amplitude, low-frequency pressure fluctuations (chugging).
Higher specific impulse than solid rocket motors and higher density-specific impulse than many liquid bipropellant engines.	Incomplete understanding of solid-fuel regression rates and motor-scaling effects for large hybrid systems.
Capability to smoothly change thrust on demand over wide ranges.	Lower fuel regression rates compared to composite solid rocket propellants
Well-suited for applications requiring throttling, command shutdown, restart, and long-duration missions with storable and nontoxic propellants.	Unpredictable changes in exposed burning areas during operation due to complex grain design configurations.

As presented in (KIM et al., 2015), conventional hybrid combustion using polymeric solid fuel, the low-fuel regression rate is due to the decrease of the heat amount from the flame zone to the fuel surface, in which the radial blowing of gasified fuel from the solid fuel surface blocks the incoming heat flux (MARXMAN; WOOLDRIGE; MUZZY, 1964). At the same time, Karabeyoglu et al. (KARABEYOGLU; CANTWELL; ALTMAN, 2001) have led to the identification of a class of paraffin-based fuels (16-50 carbon numbers, corresponding to paraffin and polyethylene waxes) of which the regression rates are 3 to 4 times higher than those of conventional polymeric fuels, indicating their great potential application.

2.2 Paraffin-LDPE Blended Fuels

Liquefying fuels such as paraffin-based fuels are widely used to obtain fuel-rich, close-to stoichiometric oxidizer-to-fuel (O/F) ratios in hybrid rockets due to their low cost and high regression rate, compared to traditional solid fuels, such as Hydroxyl-terminated polybutadiene (HTPB) and High-Density Polyethylene (HDPE) (LECCESE; CAVALLINI; PIZZARELLI, 2019; SHYNKARENKO; GONTIJO, 2020).

Paraffin, a mixture of saturated hydrocarbons (alkanes), is a by-product of the production of lubricant oil in the petrochemical industry. Constituting about 15% by weight of crude, it must be isolated to prevent crystallization at low temperatures. Its components are solid at room temperature, with melting points ranging from 50 to 70 °C. Because it is primarily composed of alkanes, it contains around 80–90% linear chains (n-paraffin) with 20–30 carbon atoms (PALOU et al., 2014).

Although chemical and physical properties can vary depending on the type of wax, its size, shape, and any additives or impurities, a general chemical structure of paraffin waxes can be seen in Figure 8. The chemical formula for paraffin is C_nH_{2n+2}, where n represents the number of carbon atoms.

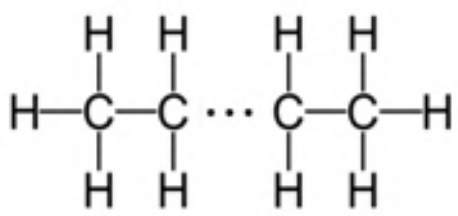

Figura 8 – Chemical structure of paraffin waxes (Own authorship).

Paraffins are distinguished by exclusively single bonds connecting the carbon atoms, forming a straight or branched chain. The interval of carbon chains can range from methane CH_4 with just one carbon atom to higher alkanes with dozens of carbon atoms. Short-chain paraffins (1-4 carbons) are gases at room temperature, medium-chain paraffins (5-16 carbons) are typically liquids, and long-chain paraffins (17 or more carbons) are solids. The physical properties of paraffins, such as boiling and melting points, increase with the length of the carbon chain due to stronger van der Waals forces in larger molecules (COELHO, 2024).

As described in (KIM et al., 2015), although the material has a high combustion rate, it has low combustion efficiency. This problem is aggravated by the difficulty in mixing it with oxidants, especially due to their high viscosity. Moreover, pure paraffin has structural integrity problems and, in several cases, poor performance due to the internal ballistics of burning propellants in hybrid rocket engines, leading to severe deformation

under storage, handling, or operational conditions due to its low melting point.

The combustion efficiency of paraffin-based fuels is lower than the usual polymeric fuel because fuel droplets generated from the melted liquid layer are not completely burned during the passage of the fuel grain port and through the exhaust nozzle (NAKAGAWA; HIKONE, 2011; ISHIGURO et al., 2011). To address this concern, many research initiatives are currently being conducted to explore the application of alternative materials as additives to paraffin wax. The use of energetic additives can improve combustion efficiency and potentially offer control over the regression rate (CANTWELL; KARABEYOGLU; ALTMAN, 2010).

The addition of LDPE is known to increase the viscosity of paraffin-based fuel and consequently increase combustion efficiency, as described by (KIM et al., 2015). For this reason, it was the material selected to compose the test specimens available at CPL. When used in small amounts, they showed an improvement in the structural properties of the grains.

LDPE is a type of alkene polymer made from the polymerization of ethylene, being chemically homologous to paraffin waxes, as both are composed of long hydrocarbon chains with similar nonpolar characteristics and thermal behavior. The chemical formula for LDPE is $(C_2H_4)_n$ and a general chemical structure can be seen in Figure 9.

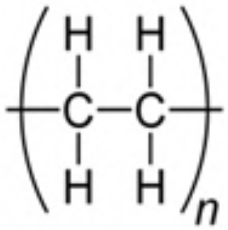

Figura 9 – Chemical structure of LDPE (Own authorship).

Based on previous studies carried out at CPL, reported by (COELHO, 2024), the addiction of LDPE offers advantages and disadvantages to the fuel. Its key benefits include increased tensile strength, improved combustion efficiency, and regulated melting efficiency. However, the material has lower chemical resistance in some applications, a tendency to permanently deform under stress and a reduction in the regression rate.

2.3 Slab Burner: Principles and Applications

A slab burner, also called a planar burner, is an engine type utilized to evaluate and characterize various types of propellant samples for hybrid and solid rocket motors. It is commonly used to understand the properties of fuels, such as physical characteristics and chemical behavior, leading to a better identification of the performance and efficiency

parameters due to its operational adaptability and compact size when compared to those of higher-scale engines.

These capabilities involve advantages in terms of the number of tests, as they can perform tests with different combustion settings effortlessly, for example, changing the oxidizer flow rate or ignition techniques, resulting in significant cost reductions during the propellant development and evaluation processes.

With these advantages in mind, the slab burner proves to be a useful tool for initial testing, providing a way to study combustion in conditions that closely resemble those of a HRM. This approach facilitates assessments and improvements with minimal propellant quantities, making it easier to study the combustion settings and confirm findings before moving on to creating a full-size fuel grain for the final engine configuration.

Moreover, the design of the combustion chamber along with the two-dimensional burning surface configuration in a slab burner provides optical access to its interior, making it well suited for research of the internal ballistics of HRE. Having one or multiple observation windows in the combustion chamber enables flame visualization and high-speed imaging of the combustion process. Analyzing these flame structures and behaviors, such as paraffin droplet entrainment and liquid layer instabilities, provides data to study various combustion phenomena in depth. Consequently, slab burners are not only cost-effective but also highly efficient for research and development in rocket propulsion.

Numerous institutions have constructed them with varying testing objectives for the development of hybrid technology. These objectives include either visualizing the combustion process through hot gas pyrolysis or full boundary layer combustion, or direct visual regression rate measurements. Hot gas pyrolysis allows the user to visualize the melt layer and any mechanical entrainment that may occur without any combustion. It can also be used to define the amount of regression that is attributed to droplet entrainment (LESTRADE; ANTHOINE; LAVERGNE, 2011; VEALE et al., 2017).

These devices share common features, but differ in specific design elements and applications. The Tables 5 and 6 explore and compare three functional slab burners: the RMA (Belgium), MOUETTE (Brussels) and KAU (South Korea), which can be seen in Figures 10, 11 and 12, respectively.

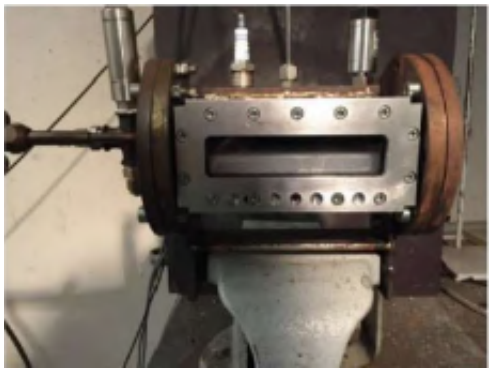

Figura 10 – RMA 2-D slab-burner (BERTOLDI et al., 2018).

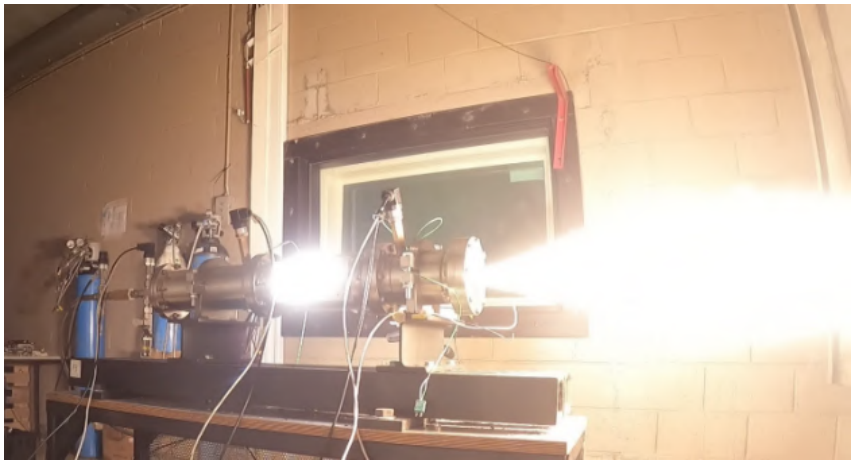

Figura 11 – : Photograph of a MOUETTE test at high-pressure conditions (KOBALD; CIEZKI; SCHLECHTRIEM,).

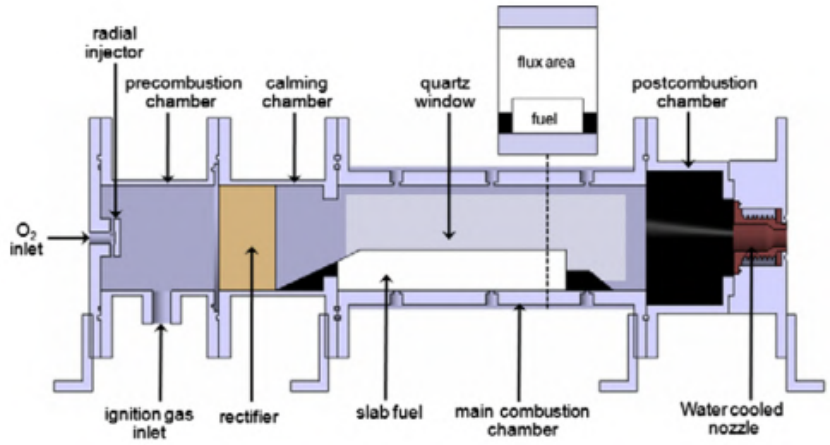

Figura 12 – Slab hybrid motor for reactive flow visualization (KIM et al., 2015).

Feature	**RMA**	**MOUETTE**	**KAU**
Primary Purpose	Parametric studies on fuel mixtures, ignition effects, and oxidizer injection.	Enhanced flexibility, modularity, and measurement quality for hybrid rocket research.	Investigating liquid film dynamics and regression rates in paraffin-based fuels.
Design Characteristics	Steel chamber with square cross-section, borosilicate glass optical access.	Cylindrical modular chamber, stainless steel/brass components, dual quartz windows.	Rectangular test section, transparent window (often covered), no nozzle, collector duct for liquid films.
Oxidizer	Liquid N_2O with a swirling injector.	Gaseous oxygen injected via a stainless steel pre-chamber and injector plate.	Gaseous oxygen via a showerhead injector with 36 holes.
Ignition Method	Gaseous oxygen and propane torch with spark plug.	Gaseous oxygen ignition, injector head for precision.	Nichrome wire surface heating, followed by gaseous oxygen.
Fuel Placement	Configurable grain placement in the chamber.	Solid fuel grain (133 mm × 74 mm × 63 mm) supported by a brass holder.	Paraffin-based fuel at bottom of the chamber, initial port height 20 mm.

Tabela 5 – Comparison between the RMA (GELAIN et al., 2022), MOUETTE (GELAIN et al., 2022) and KAU Slab burner (LEE et al., 2023) (Part 1).

Feature	**RMA**	**MOUETTE**	**KAU**
Key Components	Combustion chamber, optical window, transducer, thermocouple, flat adjustable plate.	11 modular parts: injector head, pre-chamber, window frame, nozzle insert, grain support, etc.	Honeycomb section, injector, contraction section, combustion chamber, and collector duct.
Operational Pressure	Limited by flat plate adjustment.	Supports higher pressures with modular design and graphite components.	Atmospheric pressure, no nozzle installed.
Flow Conditioning	Swirling oxidizer injector.	Pre-chamber reduces turbulence, conditions oxidizer flow.	Honeycomb for uniform flow, contraction section reduces losses.
Measurement Capability	Pressure and temperature sensors.	Enhanced measurement versatility with optical access and modular components.	Turbine flow meter, programmable controller, and DAQ system.
Test Focus	Regression rates, ignition, oxidizer dynamics.	Broad hybrid rocket research, including modularity and chamber dynamics.	Liquid film behavior, droplet entrainment, and mass transfer.

Tabela 6 – Comparison between the RMA (GELAIN et al., 2022), MOUETTE (GELAIN et al., 2022) and KAU Slab burner (LEE et al., 2023) (Part 2).

Other institutions have developed slab burners to perform a variety of combustion tests. For example, as described by (VEALE et al., 2017), ONERA and KAU investigated hot gas pyrolysis to assess the effect of liquid layer entrainment on the regression rate. By removing combustion, the effect of normal boundary layer combustion was eliminated, leaving only unstable wave formation. In addition to this, KAU compared the pyrolysis result to full combustion results.

TU and KAU also investigated the effects of the fuel viscosity on liquid layer formation and subsequent droplet entrainment. The viscosity was modified by mixing EVA and LDPE into paraffin wax, respectively.

Stanford University used a slab motor to study droplet entrainment visually, resulting in slow motion videos that clearly show droplet entrainment of the paraffin wax fuel into the oxidizer stream through the formation of waves in the liquid layer. This test stand was not intended to measure fuel regression. Finally, SPLab and Penn State University both investigated the regression rate effects of fuels doped with metalized particles,

specifically aluminum, magnesium, and lithium hydride.

The regression rate data obtained from some of these slab burner tests have been plotted on a common set of axes for comparison, as shown in Figure 13.

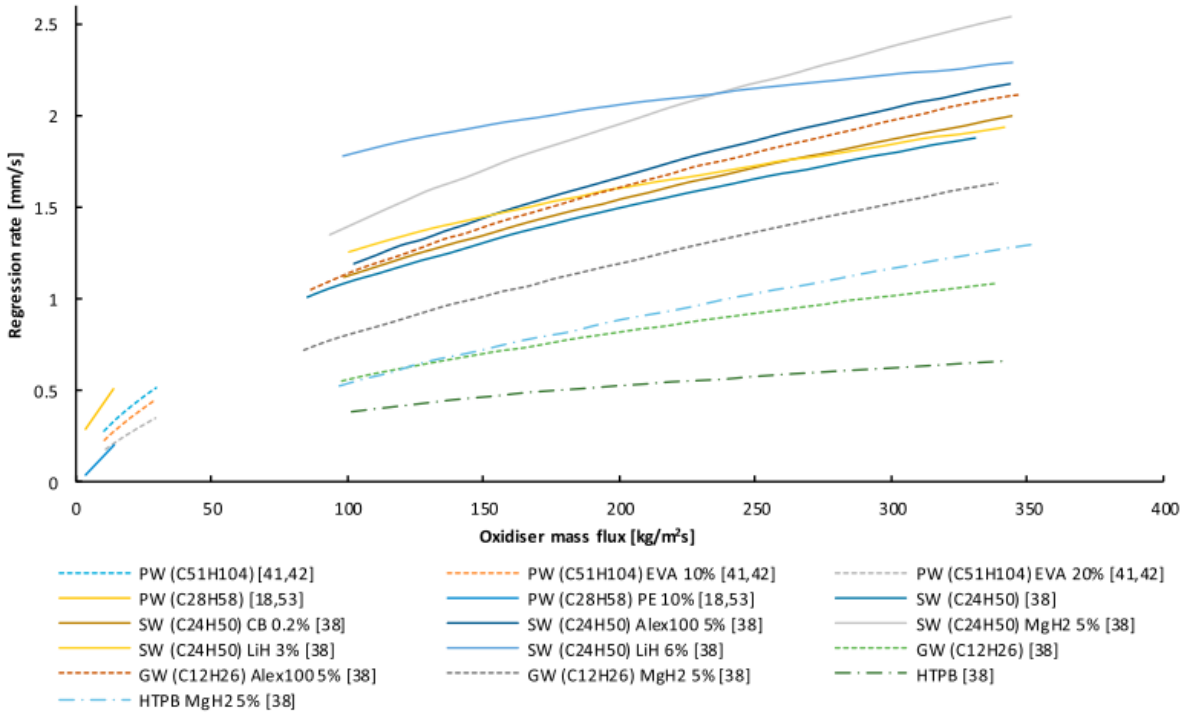

Figura 13 – 2D regression rate results for various wax samples with additives (VEALE et al., 2017).

2.4 Performance and Efficiency Parameters of Hybrid Engines

The performance of a hybrid rocket motor can be defined in terms of some performance parameters, especially by the delivered specific impulse, and depends critically on the degree of flow mixing achieved in the combustion chamber. High performance stems from high combustion efficiency is a direct function of the thoroughness with which unburned oxidizer mixes with unburned fuel (SUTTON; BIBLARZ, 2017).

The specific impulse is calculated using force per unit mass flow rate, displayed in Equation 2.6, representing the thrust per unit propellant weight flow rate. The specific impulse is essentially a vehicle system performance parameter.

$$I_s = \frac{F}{\dot{m} g_0} = \frac{u_e}{g_c} + \frac{(P_e - P_a)A_e}{\dot{m}} \tag{2.6}$$

A slab burner does not completely simulate the dynamic flow of a real engine, especially in the nozzle sections. The specific impulse depends on the thrust generated by the engine in a complete system, which includes the effect of the nozzle and the expansion of gases. Therefore, it is not a relevant parameter in this type of test.

According to (KARABEYOGLU et al., 2004), the combustion efficiency, that is, $c^\star$ efficiency, of the motor, is calculated based on Equation 2.7. The efficiency term can be used to express the degree of completion of chemical energy releases in the generation of high-temperature, high-pressure gases in combustion chambers (SUTTON; BIBLARZ, 2017).

$$\eta_c = \frac{c^\star_{act}}{c^\star_{theo}} \tag{2.7}$$

The measured characteristic velocity ($c^\star_{act}$) for each test can be estimated using the relation presented in Equation 2.8 (KIM et al., 2015).

$$c^*_{\text{act}} = \frac{p_1 A_t}{\dot{m}} = \frac{A_t \int_0^{t_b} P_c \, \mathrm{d}t}{\int_0^{t_b} \dot{m}_o \, \mathrm{d}t + \Delta m_f} \tag{2.8}$$

The characteristic velocity is only a function of propellant characteristics and combustion chamber properties, independent of nozzle configuration. Thus, it can be useful when comparing different propellant combinations for combustion chamber performance (SUTTON; BIBLARZ, 2017). The theoretical characteristic velocity can be calculated using the CEA code.

Although the regression rate does not serve as a direct indicator of combustion efficiency, it has an indirect influence by modulating the mixture ratio and combustion dynamics. From a practical perspective, the optimization of the regression rate can lead to elevated combustion efficiency within HRE.

Fuel regression rates are primarily determined by the oxidizer mass velocity, also called the oxidizer flux, which is equal to the mass flow rate of the oxidizer in a combustion port divided by the port cross-sectional area (SUTTON; BIBLARZ, 2017). Low fuel regression rates correspond to low fuel mass flow rates, leading to excess oxidizer passing through the motor, which reduces the available thrust and, therefore, reduces the overall efficiency (HIRATA et al., 2011).

The simplest method to measure temporally and spatially averaged regression rate is to measure the fuel grain mass before and after the burn, then divide by the burn time, as performed in (CAI et al., 2013; DUNN et al., 2018; KNUTH et al., 2002). (GALFETTI et al., 2013) presented an equation based on the fuel volume and burn time, as follows:

$$\dot{r} = \frac{\Delta m_f}{\rho_f t_b A_b} \tag{2.9}$$

Measuring the regression rate this way may be subject to error caused by part of the fuel mass not combusting and melting away. Another drawback to weighing the fuel grain is that it does not provide data on local and instantaneous regression rates (ZILLIAC; KARABEYOGLU, 2006).

2.5 Data Acquisition Systems and Sensors at the Chemical Propulsion Laboratory (CPL-UnB)

The Chemical Propulsion Laboratory (CPL) at the University of Brasília (UnB) is a leading national research center focused on the development of propulsion systems for rockets and jet engines. To ensure accuracy and safety in its experiments, CPL employs advanced data acquisition systems (DAQs) and a variety of sensors integrated into its testing facilities.

Multiple DAQ systems are utilized to monitor and record critical parameters during propulsion tests. These systems provide real-time data collection, essential for performance analysis and theoretical validation. Primary DAQ systems include:

- **Lynx Data Acquisition Systems**: The Lynx ADS1000 and ADS0500 models are used for high-speed, high-precision data acquisition.
- **Lynx ADS2000**: Another Lynx model designed for applications that require a higher number of channels and advanced functionalities.
- **National Instruments Data Acquisition and Control System**: The unit consists of a CompactDAQ NI cDAQ-9178 chassis, together with various modules (9208, 9213, 9237, 9266, and 9482) for flexible and scalable signal acquisition.

These systems enable the precise monitoring of variables such as pressure, temperature, thrust, and fuel flow, ensuring reliable results in propulsion testing. To support experimental activities, CPL integrates a wide range of sensors into its test benches:

- **Pressure Sensors**: Measure pressure levels in combustion chambers and propellant feed lines.
- **Temperature Sensors**: Monitor temperatures in critical components, such as injectors and engine structures.
- **Load Cells**: Used to measure thrust generated by the engines.
- **Flow Sensors**: Monitor the flow rate of liquid and gaseous propellants.

The laboratory also has testing and assembly facilities specifically designed to accommodate various experimental configurations.

- **Assembly and Control Room**: Equipped with workbench for assembly of mechanical, electrical and electronic components. It includes 75-inch monitoring screens and computers dedicated to test bench control.

- **Test Benches**: Dual horizontal test benches for rocket and ramjet engines with up to 3 kN of thrust, a vertical test bench for thrust vector control (TVC) studies, and a planar slab burner for hybrid propellant experiments.
- **Propellant Supply and Handling System**: Designed for the safe handling of liquid and gaseous oxidizers, ensuring operator safety and experimental reliability.

A schematic of the whole feeding system is shown in Fig. 14.

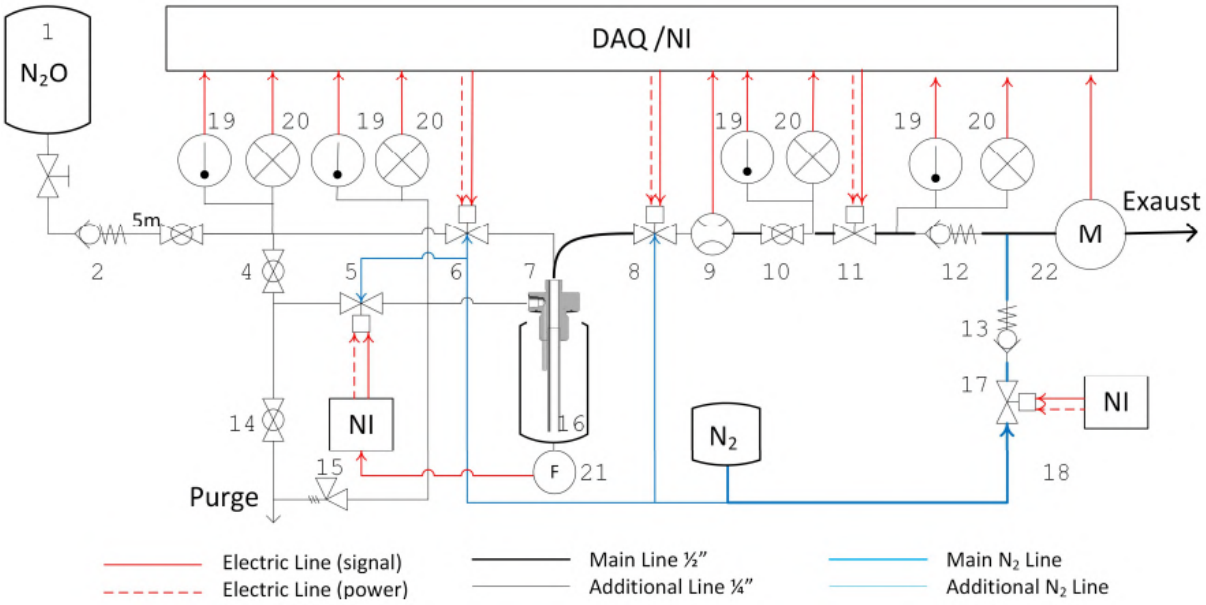

Figura 14 – System schematics (SHYNKARENKO; GONTIJO, 2020).

3 Methodology

The methodology used is part of a broader research initiative supported by the Fundação de Apoio à Pesquisa do Distrito Federal (FAPDF), with the objective of investigating the combustion behavior of paraffin-based solid fuels for hybrid rocket propulsion applications. The combustion tests were carried out using the existing infrastructure available at CPL.

The experimental hardware, including the stainless steel slab burner and the oxidizer feed system, had been previously designed and assembled within the scope of this project. Also, the solid fuel samples used in this study were previously manufactured following established procedures, as detailed in (COELHO, 2024), and stored until testing.

This chapter presents the experimental setup, including the oxidizer feed system, the slab burner configuration, and the control and sensing systems used. Additionally, it outlines the measurement procedures and data acquisition methods adopted during testing, as well as the approach used to quantify and propagate measurement uncertainties.

3.1 Experimental Setup

The data acquisition and oxidizer delivery systems were designed to support hybrid rocket motor testing with high accuracy and safety. The data acquisition system is based on the CompactDAQ® platform by National Instruments, which is central to CPL's instrumentation architecture. This modular system is capable of real-time monitoring and control of experimental parameters. The CompactDAQ chassis interfaces with the computer via USB, Ethernet, or Wi-Fi, and is compatible with various input/output modules tailored for temperature, pressure, voltage, and current measurements. Integration with LabVIEW software enables the development of customized applications for data collection, analysis, and visualization.

The primary sensors used were a turbine-type flow meter (volumetric, in liters), thermocouples, and Danfoss MBS pressure transducers. The thermocouples monitored oxidizer temperatures at key points throughout the feed system—filling line, purge line, and both upstream and downstream of the main control valve—while the pressure transducers measured values at the same locations. These sensors were selected for their robustness, local market availability, and cost-effectiveness, especially for scenarios involving cryogenic or bi-phase oxidizers like nitrous oxide.

The oxidizer feed system incorporated four on/off valves: pneumatically actuated solenoid valves (3, 10), manual shut-off valves (5), and stop valves (7, 8), which ensured

safe operations during oxidizer filling, discharging, ignition, and nitrogen purging. A high-pressure regulator (2) was installed in the oxidizer tank to control the flow rate, which was regulated via the control valve (6) placed just before the combustion chamber. The tank (1) was pressurized using an external air compressor, ensuring a stable oxidizer supply to the motor.

Figure 15 shows a schematic of the oxidizer feed system, highlighting the layout and interaction between key components.

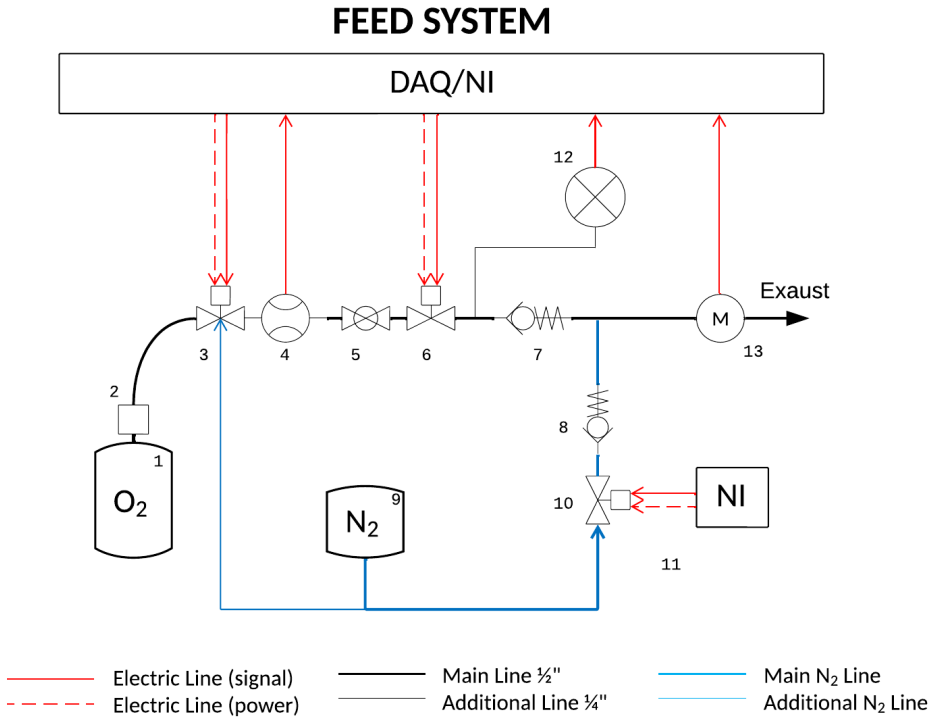

Figura 15 – System schematics (Adapted from (SHYNKARENKO; GONTIJO, 2020)).

Table 7 summarizes the main elements of the oxidizer feed system and their respective functions.

Element	Description	Function
Pressure Sensors (12)	Located in the feed lines, tank, and after the control valve.	Measure oxidizer thermodynamic properties to monitor valve openings and flow rate.
Tank (1)	Equipped with a doubled dip tube and pressurized externally.	Stores and delivers gaseous oxygen.
High Pressure Regulator (2)	Installed in the tank.	Controls oxygen pressure for safe and stable feed.
Flow Meter (4)	Turbine-type sensor.	Measures volumetric flow rate of oxidizer.
Solenoid Valves (3, 10)	Pneumatically actuated and electrically controlled.	Handle oxidizer feed and nitrogen purge.
Stop Valves (7, 8)	Installed in oxidizer and nitrogen lines.	Prevent reverse flow during operation.
Manual Valves (5)	Located throughout the system.	Isolate segments of the line when offline.
Control Valve (6)	Positioned before the combustion chamber.	Regulates oxidizer flow entering the slab burner.
Nitrogen Purge	End-of-test safety system.	Removes oxidizer remnants and extinguishes combustion.

Tabela 7 – Summary of System Elements and Functions. Adapted from (SHYNKARENKO; GONTIJO, 2020).

To ensure the reliability of the experimental data, estimated uncertainties were established based on equipment specifications and prior validation studies: ±1.5% for pressure readings, ±1°C for temperature and ±2.5 ms for timing accuracy (SHYNKARENKO; GONTIJO, 2020). The volumetric flow rate of oxidizer was measured using an Omega FTB793 turbine-type flowmeter, specified to have a linear accuracy of ±2% of the reading (OMEGA Engineering, Inc., 2018).

3.1.1 Combustion Procedure and Ignition System

Each test was initiated using a nichrome-wire ignition system designed to preheat the surface of the paraffin fuel and initiate combustion. A 0.5 mm thick nichrome wire was affixed along a groove located at the base of the fuel sample, ensuring localized and consistent heating. The wire was electrically connected to a 12 V battery, and the current passing through it caused rapid resistive heating. This thermal input was sufficient to melt a thin surface layer of the paraffin fuel.

Once the paraffin began to melt, the main oxidizer control valve was opened, allowing gaseous oxygen to enter the combustion chamber and support ignition. The ignition process lasted approximately 3 seconds. Figure 16a and Figure 16b illustrate the ignition configuration used in the tests.

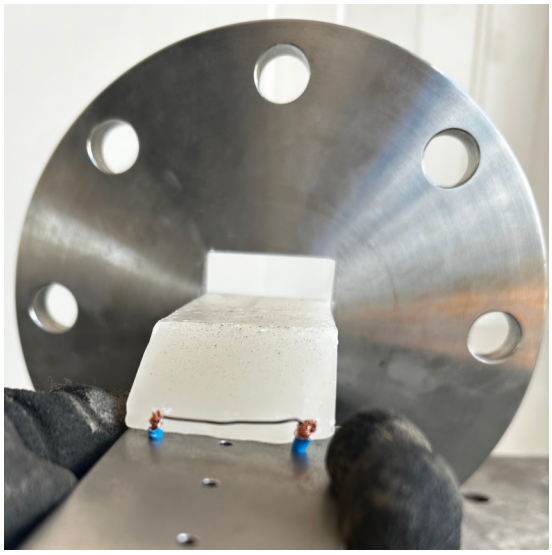

(a) Nichrome wire positioned near the paraffin surface.

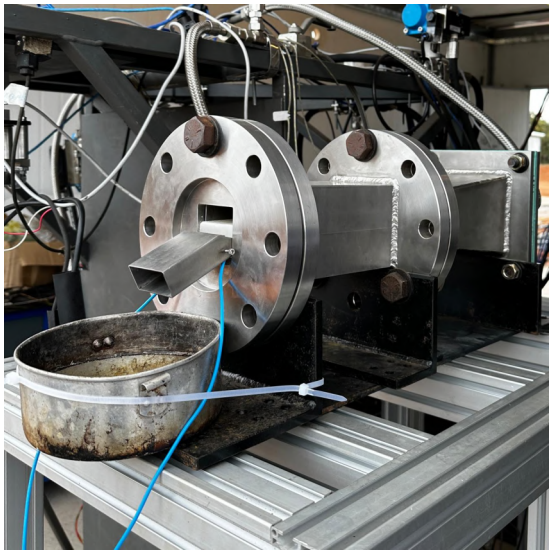

(b) Wiring connected to a 12V battery prior to firing.

Figura 16 – Ignition system configuration (Own authorship).

The mass of fuel consumed during ignition phase was considered negligible and was neglected from regression rate calculations. This assumption aligns with prior literature (LEE et al., 2023), which confirmed that the ignition losses do not significantly affect the overall fuel regression behavior.

After combustion, the condensed liquid paraffin film, generated by surface melting during the test, was collected using a small container affixed to the rear end of the slab burner. This container allowed the collection and measurement of the mass of re-condensed paraffin, used to determine the liquid film regression rate, as detailed in Section 3.3.

The burn duration was defined by the interval during which oxidizer flow was actively delivered and was designed to last approximately 5 seconds, which was considered sufficient to establish stable combustion and ensure measurable fuel regression. However, due to manual operation of the main valve and the lack of many verification videos, the actual burn time varied between 5 to 7 seconds. This variation was accounted for in all mass flow and regression rate calculations, where the actual burn time (t_b) was determined individually for each test.

3.2 Propulsion System and Fuel Configuration

The propulsion system used was a stainless-steel slab burner designed and fabricated by CPL. The conceptual design of this burner is shown in Figure 17, and its main components are summarized in Table 8.

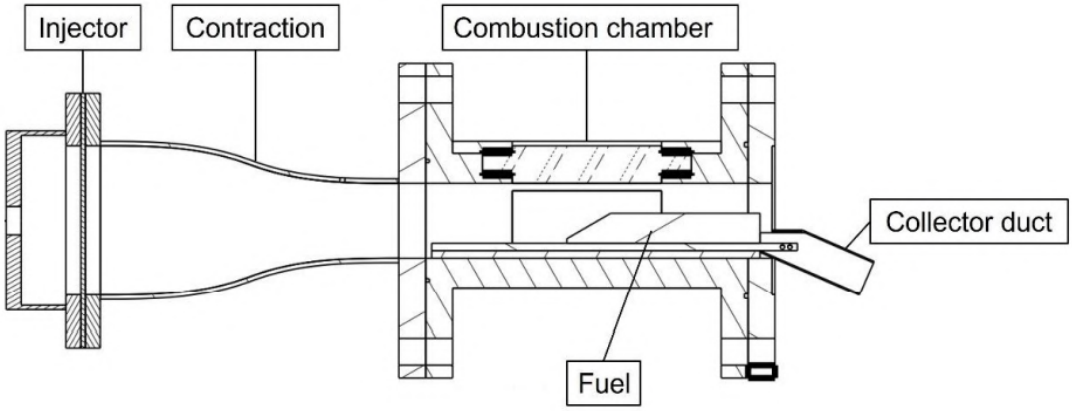

Figura 17 – Configuration of slab hybrid motor (LEE et al., 2023).

Tabela 8 – Main Components (Own authorship).

Component	**Description**
Injector Section	Showerhead-type injector with 36 holes of 2 mm diameter, sealed with NBR gaskets.
Contraction Section	Ensures flow uniformity and reduces frictional losses.
Combustion Chamber	Main chamber where the oxidizer and fuel interact and combustion occurs.
Collection Duct	Guides and directs exhaust gases post-combustion.

The slab burner was designed to be compatible with the slab burner developed at KAU, allowing direct comparison with results from (LEE et al., 2023). Due to its robust stainless-steel construction, the burner was significantly oversized to guarantee mechanical and thermal integrity. Given its substantial weight, it was positioned directly onto the aluminum test bench without mechanical restraints. Since the configuration of the slab burner does not generate axial thrust during operation, this configuration was safe and effective.

Figures 18a and 18b show different views of the assembled burner.

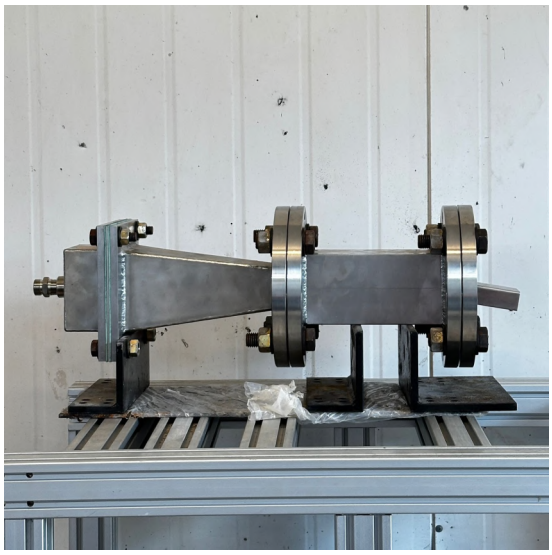

(a) Side view of the assembled motor.

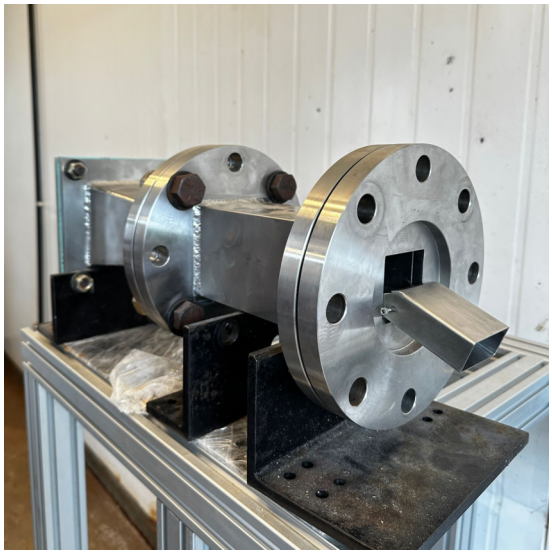

(b) Back view of the assembled motor.

Figura 18 – Assembled motor outside the test bench (Own authorship).

The burner was configured to accommodate the solid fuel slabs placed in the open combustion chamber. This geometry deviated from conventional cylindrical ports, allowing the study of two-dimensional regression rates.

The solid fuel slabs used were fabricated using paraffin wax, with and without LDPE additives. Each fuel type consisted of four samples, whose individual dimensions and masses were measured using a digital caliper (resolution: 0.01 mm) and an analytical balance (resolution: 0.1 g), respectively. The wet surface area (A_w) was computed as the sum of the top flat surface and the inclined ramp face, which are the active burning areas.

Figure 19 shows the schematic drawing used for dimensional reference.

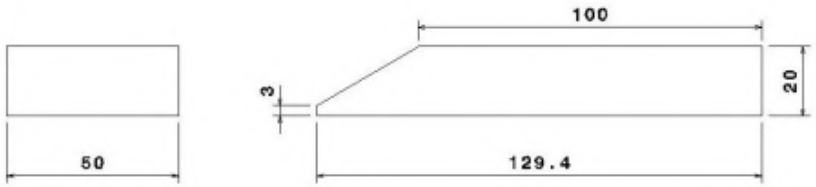

Figura 19 – Fuel grain schematic (GUEDES, 2024).

Table 9 summarizes the dimensional characteristics of the fuel samples by formulation, presenting the mean and standard deviation for each parameter. These results were derived from the full dataset provided in Appendix A, containing individual measurements and calculated errors for all 12 samples.

The relative error (%) for each dimension was computed by comparing the measured values to the reference dimensions shown in the Figure 19. For each sample, the absolute error was determined and then normalized by the expected value.

Tabela 9 – Average dimensions and standard deviations by fuel type (Own authorship).

Fuel Type	Height (mm)		Width (mm)		Length (mm)		Incl. Thick. (mm)		Top Sec. L (mm)		Weight (g)		Burning Area (m²)	
	Mean	Std	Mean	Std	Mean	Std	Mean	Std	Mean	Std	Mean	Std	Mean	Std
PR100	20.28	0.36	49.53	0.44	127.26	0.95	6.10	2.24	99.32	2.02	98.95	7.56	0.01	0.00
PR90PE10	20.23	0.56	49.19	0.12	126.12	1.57	6.01	2.10	99.87	1.47	99.20	7.72	0.01	0.00
PR95PE05	20.46	0.38	49.12	0.36	126.36	0.87	7.40	1.60	99.70	0.19	105.12	2.94	0.01	0.00

Statistically significant variations were observed in the sample mass and inclined thickness, reflecting the influence of LDPE concentration on fuel density. Due to the manual manufacturing, the samples presented visible imperfections and internal bubbles, which influenced the experimental density and introduced measurement uncertainty, as discussed in Section 3.5.

The raw materials processed in the fabrication of PR100, PR90PE10 and PR95PE05 slab fuels are described in Table 10.

Tabela 10 – Properties of manufactured blended paraffin slab fuels (COELHO, 2024).

Name	$\mathbf{C_xH_y}$	**m** (g/mol)	**Melting Point (ºC)**	**Density (g/cm^3)**
SOLVEN 140 Wax	$C_{21}H_{44}$	296.6	59	0.791
Hanwha Chemical Co LDPE	$(C_2H_4)_n$	–	110	0.921

Note: The symbol – indicates unavailable data.

Some parameters were experimentally collected regarding the manufactured fuel samples. All this data can be seen in Table 11.

Tabela 11 – Experimental Parameters of Blending Paraffin Fuels Developed at CPL (COELHO, 2024).

Parameter	**PR100**	**PR95PE05**	**PR90PE10**
Dimensional ρ (kg/m^3)	906	906	907
Experimental ρ (kg/m^3)	830	840	875
Young's Modulus (MPa)	135.307	79.564	107.000
Compressive Strength (MPa)	2.330	1.890	2.370

Visual inspection of samples:

(a) PR100 (b) PR95PE05 (c) PR90PE10

Figura 20 – An individual sample of each fuel category (Own authorship).

3.3 Calculation of Propellant Flow and Regression Rates

To transform the raw experimental data into relevant combustion parameters, a set of physical relationships was applied to compute the oxidizer mass, oxidizer and fuel mass flow rates, and the total propellant mass flux and the regression rates.

The mass of oxidizer injected during each test was calculated using the ideal gas law. Instead of using the universal gas constant R_u (8,31447 J/mol · K) and the molar mass of oxygen ($M = 32$ g/mol), the specific gas constant for oxygen ($R = 259.8$ J/kg · K) was adopted, following Equation 3.1.

$$\rho_{ox} = \frac{P}{RT} \tag{3.1}$$

Here, P is the absolute pressure (in Pascals), T is the absolute temperature (in Kelvin), and R is the specific gas constant for oxygen. All temperature and pressure readings used were obtained from the sensors installed upstream of the control valve. Once the oxidizer density ρ_{ox} was determined, the oxidizer mass was calculated by multiplying the density by the measured oxidizer volume (V), obtained from the turbine flow meter.

$$m_{ox} = \rho_{ox} \cdot V \tag{3.2}$$

The oxidizer mass flow rate was then obtained by dividing the oxidizer mass by the burn time t_b:

$$\dot{m}_{ox} = \frac{m_{ox}}{t_b} \tag{3.3}$$

The mass flow rate of the fuel was computed from the initial and final weights of the fuel slabs, and the burn time t_b:

$$\dot{m}_f = \frac{\Delta m_f}{t_b} \tag{3.4}$$

Following the same order, the mass flow rate of the liquid film was calculated from the the collected mass of melted paraffin (m_c) and the burn time t_b:

$$\dot{m}_{lf} = \frac{m_c}{t_b} \tag{3.5}$$

Using these mass flow rates and the port cross-sectional area A_{port}, seen in Figure 21, the total propellant mass flux was:

$$G_{tot} = \frac{\dot{m}_{ox} + (\dot{m}_f - \dot{m}_{lf})}{A_{port}} \tag{3.6}$$

The total regression rate, representing the net consumption of the fuel layer during the firing test, was calculated using:

$$\dot{r}_{tot} = \frac{\Delta m_f}{\rho_f A_w t_b} \tag{3.7}$$

To isolate the effect of the entrained liquid paraffin film, the liquid film regression rate was computed using the following relation:

$$\dot{r}_{lf} = \frac{m_c}{\rho_f A_w t_b} \tag{3.8}$$

Here, ρ_f is the fuel density, and A_w is the exposed burning surface area.

Lastly, the vaporization and droplet entrainment contribution was isolated by subtracting the liquid film contribution:

$$\dot{r}_{v+e} = \dot{r}_{tot} - \dot{r}_{lf} \tag{3.9}$$

For better visualization, a schematic of the test chamber cross section area with the fuel slab coupled is shown in Figure 21. In all cases, the cross section variation caused by the fuel consumption is neglected and only the initial geometrical dimensions are considered.

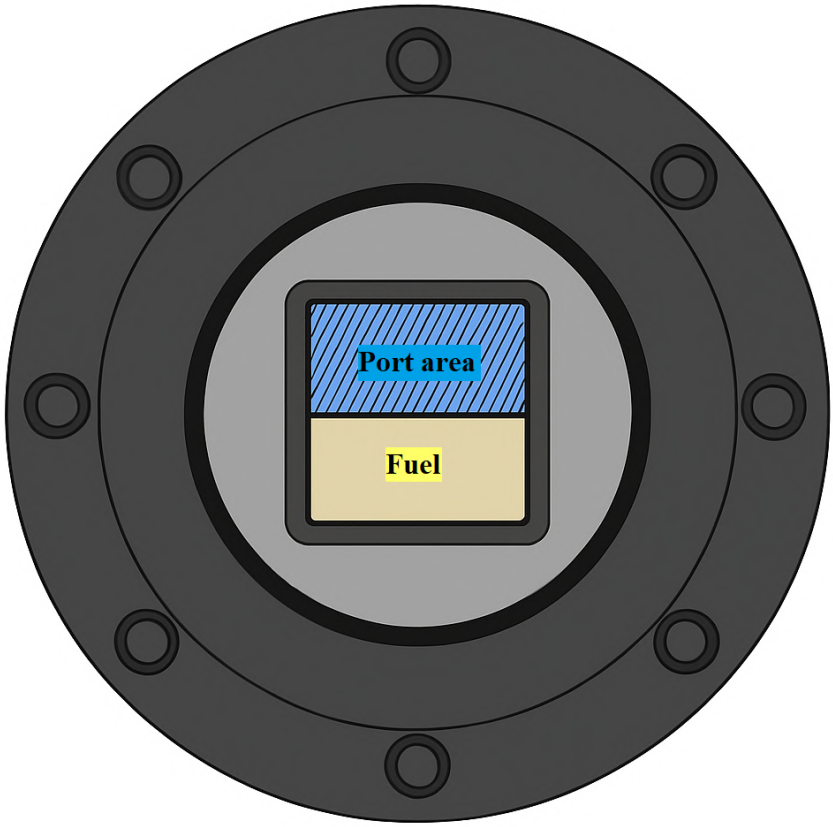

Figura 21 – Cross-section for port area evaluation (Own authorship).

Figure elements:

- **Blue striped area:** Cross-sectional area used for G_{tot} calculation.
- **Yellow region:** Fuel slab properly positioned before the combustion tests.
- **View:** Cross-section of the combustion chamber outlet.

Following the same experimental conditions as (LEE et al., 2023), no nozzle was installed in the test setup because these experiments were conducted to measure the mass transfer rate of a liquid film flowing on the solid fuel surface at the rear of the fuel, and, therefore, the experiments will be carried out under atmospheric pressure and restricted velocity conditions.

3.3.1 Curve Fitting Method for Regression Rate

To better represent the trend of the total regression rate data and mitigate the effects of experimental dispersion, a curve fitting approach was used. The classical empirical model for hybrid rocket fuel regression was applied, in which the regression rate is related to the oxidizer mass flux (G_{ox}) through the power-law relationship in Equation 3.10.

$$\dot{r}_{\text{tot}} = a \cdot G_{\text{ox}}^{n} \tag{3.10}$$

The parameters a and n were determined by performing a nonlinear curve fit to the experimental data obtained at CPL, using Python (Appendix C), which applies a least-squares optimization to find the best-fit coefficients. This fitted curve was used as a reference trendline to compare the three fuel formulations and to evaluate the consistency of the measurements.

This method minimizes the sum of the squares of the residuals between the experimental values and the model predictions. The nonlinear least squares approach makes possible to fit complex models in which the parameters appear in nonlinear form, as is the case with the exponent n. The optimization algorithm iteratively adjusted the parameters using the Levenberg–Marquardt method, a standard technique that combines the gradient descent and Gauss-Newton approaches to efficiently converge toward the minimum error.

3.4 Safety Standards and Test Preparation Guidelines

The safety of propulsion system testing is an extremely important topic and is widely covered in (NASA, 2011). Additionally, CPL security parameters and guidelines are consolidated, as described in (SHYNKARENKO; GONTIJO, 2020). The use of automated

systems for continuous monitoring reduces the risk of human errors in vital operational responsibilities during tests, especially in high-pressure settings.

Oxygen is one of the most secure rocket oxidizers because it has a non-corrosive nature. But, its reactivity increases with pressure, temperature, and concentration. Although oxygen is reactive under normal conditions, many substances that do not ignite in standard air can catch fire and burn intensely in oxygen-rich atmospheres, exhibiting lower ignition energy and faster combustion rates. Gaseous oxygen, being a small diatomic molecule, can also infiltrate porous materials, as foam insulation and fabrics.

Paraffin is also a reliable fuel that does not present risks of spontaneous ignition or explosion at room temperature. This characteristic makes it safer to manage than more volatile fuels.

In the presence of oxygen, it is essential to implement safety measures, as it can build up in the environment. Individuals exposed to high levels of gaseous oxygen, inadvertently or during fueling operations, should remain outdoors for a minimum of 30 minutes to facilitate its dissipation and dilution from their body, clothing and skin (NASA, 1996).

Additionally, the testing zone is restricted during its operation, and only those with previous authorization are allowed on the premises. The use of automatic and safety valves for propellant delivery is another safeguard, as they prevent unwanted backflow and ensure proper flow management. Also, the lines that provide the oxidizer are kept free of any organic materials that might ignite, and the testing area includes free airflow to stop the build-up of flammable gas concentrations.

To guarantee the proper functioning of all elements within the system prior to testing, automated verification are conducted, for example: evaluations of power levels, valve responsiveness, and the operation of low-pressure sensors. Also, the system is designed to automatically cease testing if there is a power outage or malfunctioning of any critical component.

These measures ensure that the propulsion tests are performed safely, minimizing risks to equipment, personnel, and the environment. In addiction, a pressure relief system was added to the oxidizer supply system, allowing the pressure in the different engine subsystems to be reduced in the event of a failure. The test sequence for the hybrid slab burner can be seen in Figure 22.

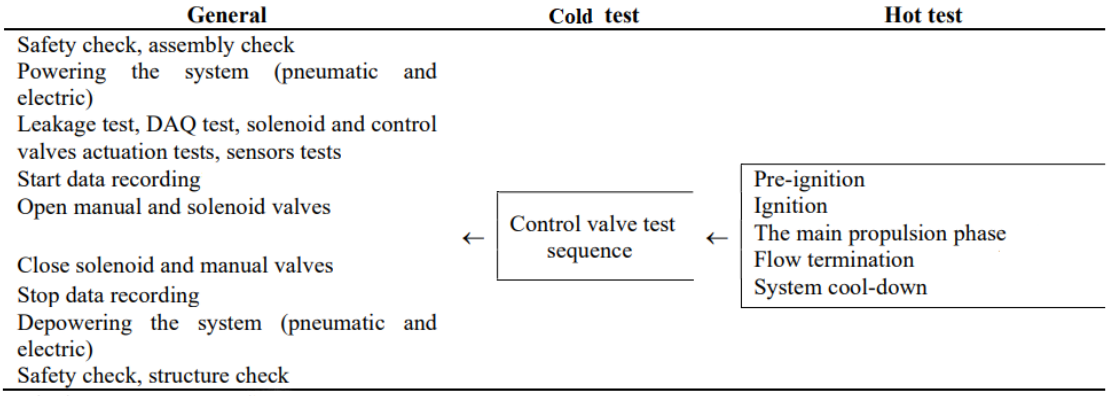

Figura 22 – Test sequence for the hybrid slab burner. Adapted from (SHYNKARENKO; GONTIJO, 2020).

3.5 Measurement Errors and Propagation of Uncertainty

This section presents the primary sources of experimental uncertainty and describes the methodology used to propagate these uncertainties through derived variables, including regression rate ($\dot{r}$), fuel and oxidizer mass flow rates ($\dot{m}_f$, $\dot{m}_{ox}$), and total mass flux (G_{tot}).

To estimate the uncertainty in the calculated quantities, the standard method of error propagation using partial derivatives was used. For a general function $f(x_1, x_2, \ldots, x_n)$, the total uncertainty is given by:

$$\delta f = \sqrt{\left(\frac{\partial f}{\partial x_1} \cdot \delta x_1\right)^2 + \cdots + \left(\frac{\partial f}{\partial x_n} \cdot \delta x_n\right)^2} \tag{3.11}$$

This approach assumes that all individual uncertainties δx_i are independent and random.

Fuel Mass Loss: The fuel mass consumed during combustion is calculated by the difference between the pre- and post-test weight of the samples:

$$\Delta m = m_{\text{before}} - m_{\text{after}} \tag{3.12}$$

Assuming the uncertainty in each measurement is taken as half the resolution ($\delta m = 0.05$ g). Thus, the uncertainty in the mass difference becomes:

$$\delta(\Delta m) = \sqrt{2} \cdot \delta m \approx 0.0707 \text{ g} \tag{3.13}$$

Burning Surface Area: The burning area (A_w) is computed as a rectangular surface ($A = b \cdot h$), where b and h represent the measured base and height of the cross-section area. Applying uncertainty propagation:

$$\delta A = \sqrt{(h \cdot \delta b)^2 + (b \cdot \delta h)^2} \tag{3.14}$$

Here, $\delta b = \delta h = 0.005$ mm, based on the caliper resolution.

Regression Rate: The total regression rate is calculated using:

$$\dot{r} = \frac{\Delta m}{\rho_f A_w t_b} \tag{3.15}$$

where ρ_f is the experimental density of the fuel, A_w is the burning area, and t_b is the burn time. Its uncertainty is given by:

$$\delta \dot{r} = \sqrt{\left(\frac{1}{\rho A_w t} \cdot \delta(\Delta m)\right)^2 + \left(\frac{\Delta m}{\rho A_w^2 t} \cdot \delta A_w\right)^2} \tag{3.16}$$

Fuel Mass Flow Rate: The fuel mass flow rate is:

$$\dot{m}_f = \frac{\Delta m}{t_b} \tag{3.17}$$

with propagated uncertainty:

$$\delta \dot{m}_f = \frac{\delta(\Delta m)}{t_b} \tag{3.18}$$

Oxidizer Mass Flow Rate: The mass of oxidizer injected was calculated using the ideal gas law, where the density is estimated from:

$$m_{ox} = \rho_{ox} \cdot V = \frac{PV}{RT} \tag{3.19}$$

Therefore, the oxidizer mass flow rate is:

$$\dot{m}_{ox} = \frac{PV}{RTt_b} \tag{3.20}$$

with the associated relative uncertainty:

$$\frac{\delta \dot{m}_{ox}}{\dot{m}_{ox}} = \sqrt{\left(\frac{\delta V}{V}\right)^2 + \left(\frac{\delta P}{P}\right)^2 + \left(\frac{\delta T}{T}\right)^2} \tag{3.21}$$

The uncertainties used were: $\delta V = 0.02V$ (flowmeter), $\delta P = 0.015P$, and $\delta T = 1$ K.

Total Propellant Mass Flux: Finally, the total mass flux is calculated as:

$$G_{tot} = \frac{\dot{m}_{ox} + (\dot{m}_f - \dot{m}_{lf})}{A_{port}} \tag{3.22}$$

The corresponding uncertainty is given by:

$$\delta G_{\text{tot}} = \sqrt{\left(\frac{\delta \dot{m}_{ox}}{A_{port}}\right)^2 + \left(\frac{\delta \dot{m}_f}{A_{port}}\right)^2 + \left(\frac{\delta \dot{m}_{lf}}{A_{port}}\right)^2 + \left(\frac{(\dot{m}_{ox} + (\dot{m}_f - \dot{m}_{lf})) \cdot \delta A_{port}}{A_{port}^2}\right)^2} \tag{3.23}$$

Unquantifiable Errors: Despite all the careful measurements performed, certain human and procedural errors were not included in the numerical propagation. The main reason for this is the difficulty in accurately determining the errors associated with them. These include:

- **Incomplete residue recovery:** After each test, the solid fuel residues adhered to the chamber walls were manually removed. Partial adhesion or uncollected residue introduces uncertainty in post-combustion mass measurements.
- **Fuel film collection losses:** The melted paraffin collected at the rear of the slab burner may not have been entirely contained within the collection pan, especially due to splashing or adhesion, leading to possible underestimation of the liquid film mass.
- **Manual handling errors:** The actions made by the operator while weighing, moving, and placing the fuel samples add to the uncertainty of the test.
- **Burn time estimation:** Only 3 out of 12 tests were filmed with the flow meter clearly visible in the video frame, allowing for precise identification of oxidizer flow initiation and cutoff. Due to that, the exact duration of oxidizer injection is estimated.

Despite the fact that these errors were not part of the official uncertainty propagation, they are recognized as possible factors influencing the overall variability of the data.

Use of Experimental Fuel Density: The regression rate calculations presented in this work rely on the experimental density of each fuel sample rather than a theoretical or

dimensionally estimated value. This choice was driven by the presence of manufacturing imperfections and was further supported by previous findings from (COELHO, 2024), who conducted a detailed comparison between dimensionally predicted and experimentally measured densities of the fuel samples. His results revealed clear discrepancies between the two methods. As noted by the author, "The graph effectively highlights the discrepancy between dimensional predictions and experimental results, suggesting that the actual material properties vary with composition, which is not captured by the dimensional analysis."

By adopting the experimental density, this work ensures more accurate reflection of the actual burning behavior, at the cost of moving away from theoretical comparisons. This is particularly important in manually fabricated slabs, where visual imperfections are frequently observed.

Figure 23 shows two sample images highlighting typical defects found on the surface of the fuel slabs, justifying the use of direct measurements in place of theoretical values.

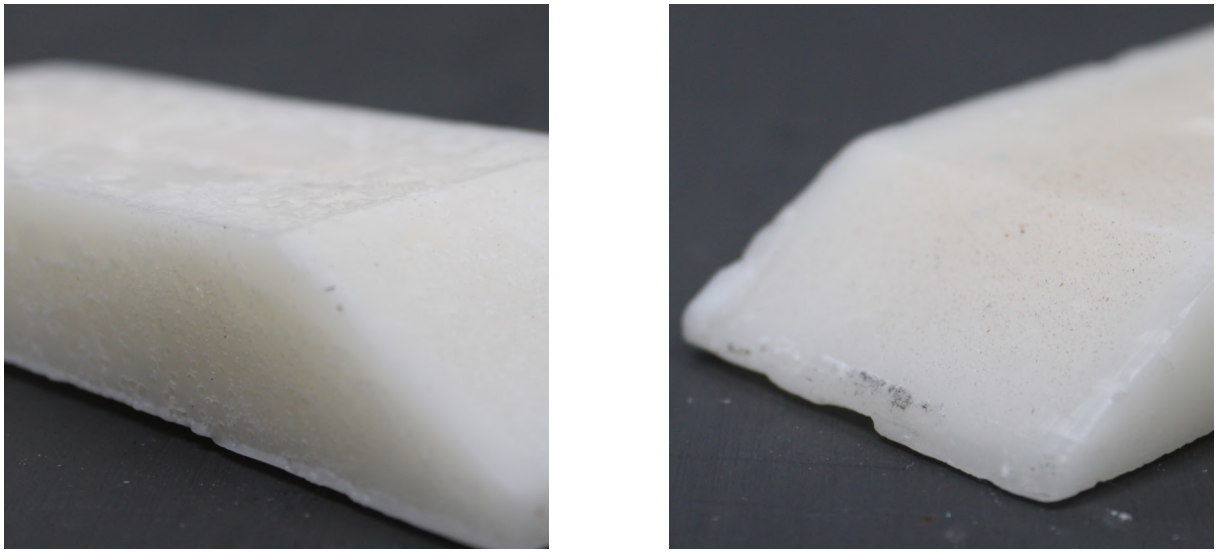

(a) Visible air bubbles on paraffin fuel surface.

(b) Surface roughness and defects due to manual casting.

Figura 23 – Examples of imperfections observed in the fuel samples (Own authorship).

Given the irregularities observed in the burn pattern of the fuel slabs, particularly the occurrence of underburn and sideburn effects that extended beyond the theoretical combustion surface, the uncertainty in the burning area could not be reliably determined through geometric propagation alone. To address this, a conservative approach was adopted in which the uncertainty in the total regression rate was estimated as 10% of its calculated value. This percentage reflects the approximate uncertainty attributed to deviations in the actual burning surface area and allows for more realistic error bars.

4 Results and Discussion

This chapter presents the experimental results obtained during the firing tests conducted at CPL and compares them with previous similar experimental findings in the literature. The main parameter analyzed is the fuel regression rate, decomposed into total regression rate ($\dot{r}_{\mathrm{tot}}$), liquid film regression rate ($\dot{r}_{\mathrm{lf}}$), and the component attributed to vaporization and droplet entrainment ($\dot{r}_{\mathrm{v+e}}$). These rates are plotted as a function of the total propellant mass flux (G_{tot}).

4.1 Literature and Theoretical Comparison

Figures 24, 26 and 28 show the regression rates obtained for the fuels PR100, PR95PE05 and PR90PE10, respectively. The data collected at CPL are compared against those reported by (LEE et al., 2023), who conducted similar experiments using the same slab burner and fuel configuration, but different range of G_{tot}.

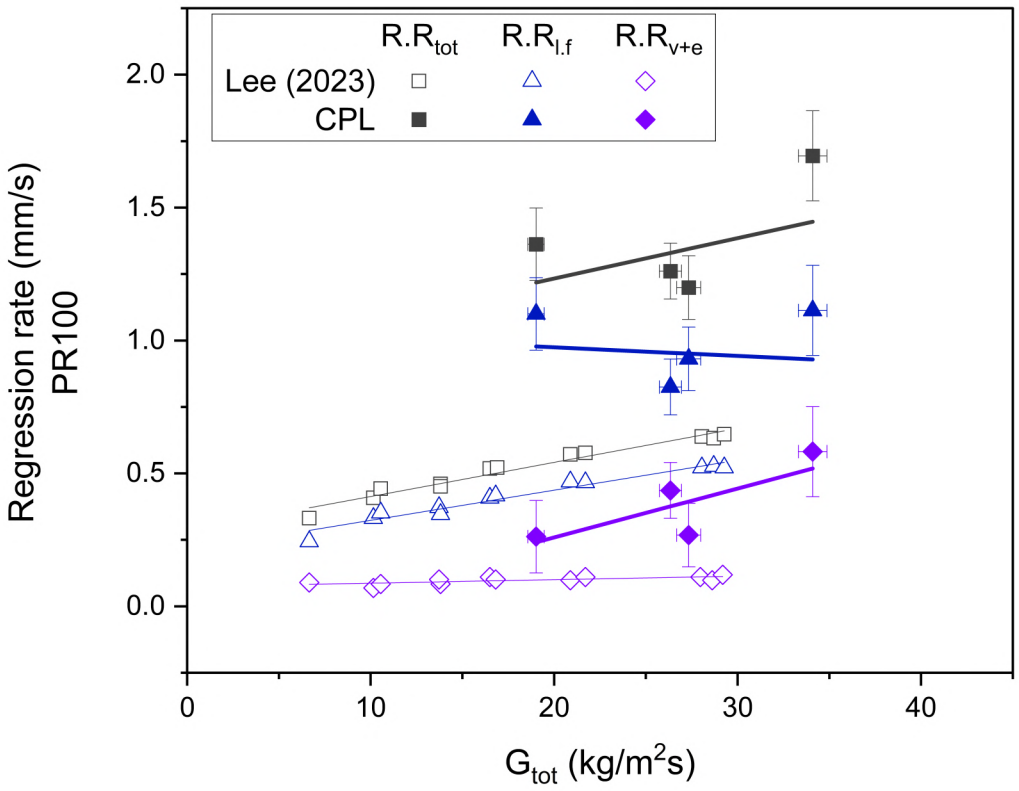

Figura 24 – Regression rates for PR100 fuel (Own authorship).

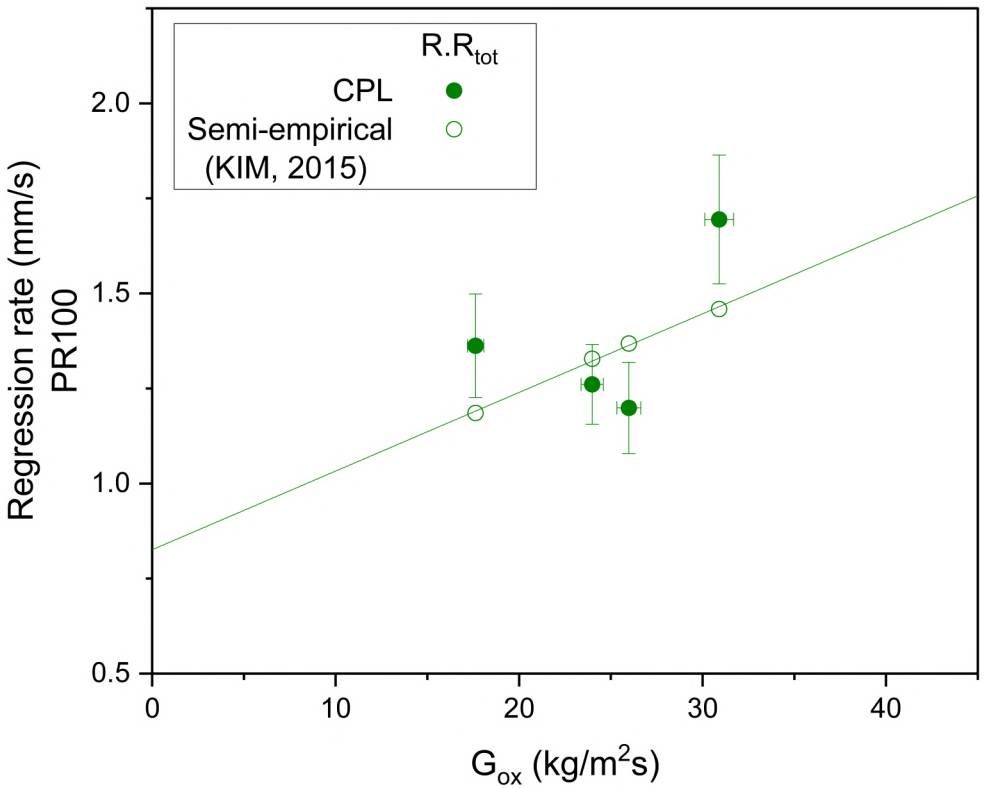

Figura 25 – Regression rate comparison with semi-empirical values for PR100 fuel (Own authorship).

Figure 25 shows the experimental regression rate data along with the fitted curve and the theoretical regression rate values for each G_{ox}, as described in Section 2.1. The fitted regression equation obtained from the four experimental points is:

$$\dot{r}_{\text{tot}} = 0.446 \cdot G_{\text{ox}}^{0.355} \tag{4.1}$$

This curve captures the overall trend of the measured values, reducing the effect of experimental scatter and allowing comparison with other sources. The fitted parameters are within the expected range for pure paraffin fuels.

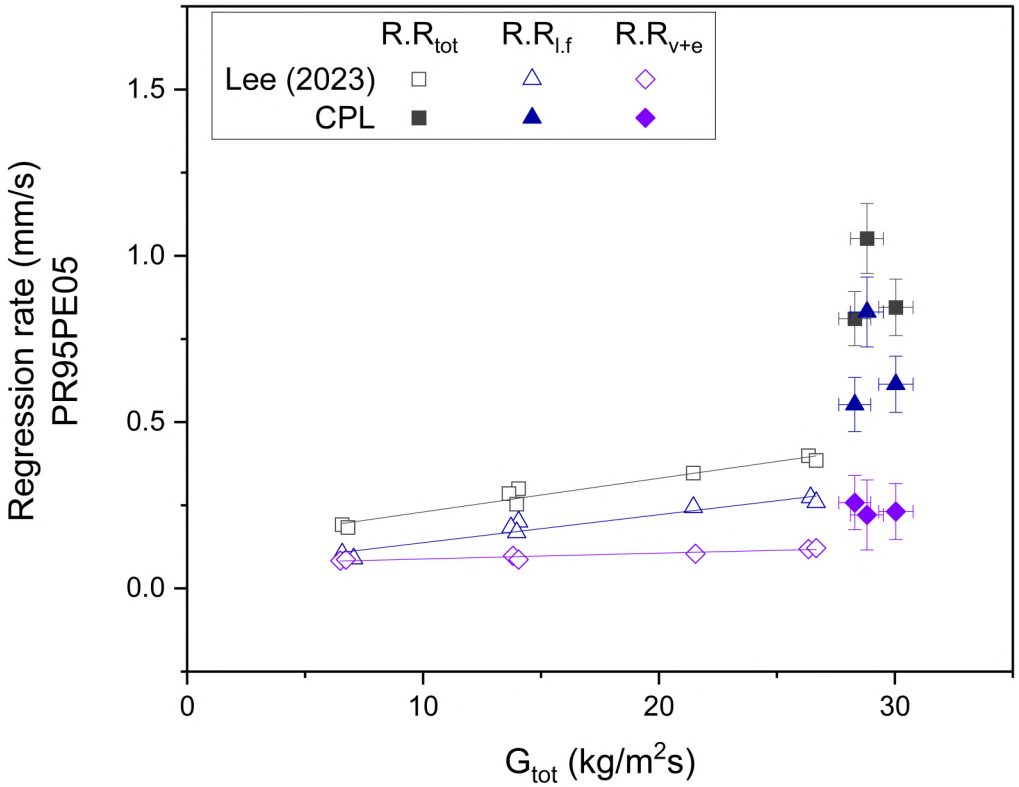

Figura 26 – Regression rates for PR95PE05 fuel (Own authorship).

In the case of the PR95PE05 fuel blend, the regression rate data presented more scattered results compared to the other compositions. Initially, four test points were available, but one of them showed an anomalous trend that resulted in an nonphysical negative exponent when doing a fitting curve. For that reason, this point was ignored to maintain the physical reliability of the analysis.

With the remaining three reliable data points, it was not possible to perform a four-point power-law fitting of the regression rate formula. As a result, no regression equation was determined for this composition. Still, the available data indicate a trend consistent with theoretical expectations, suggesting a moderate increase in regression rate with oxidizer mass flux. Additional experiments are required to complete the data and enable a more precise characterization of this LDPE concentration effects.

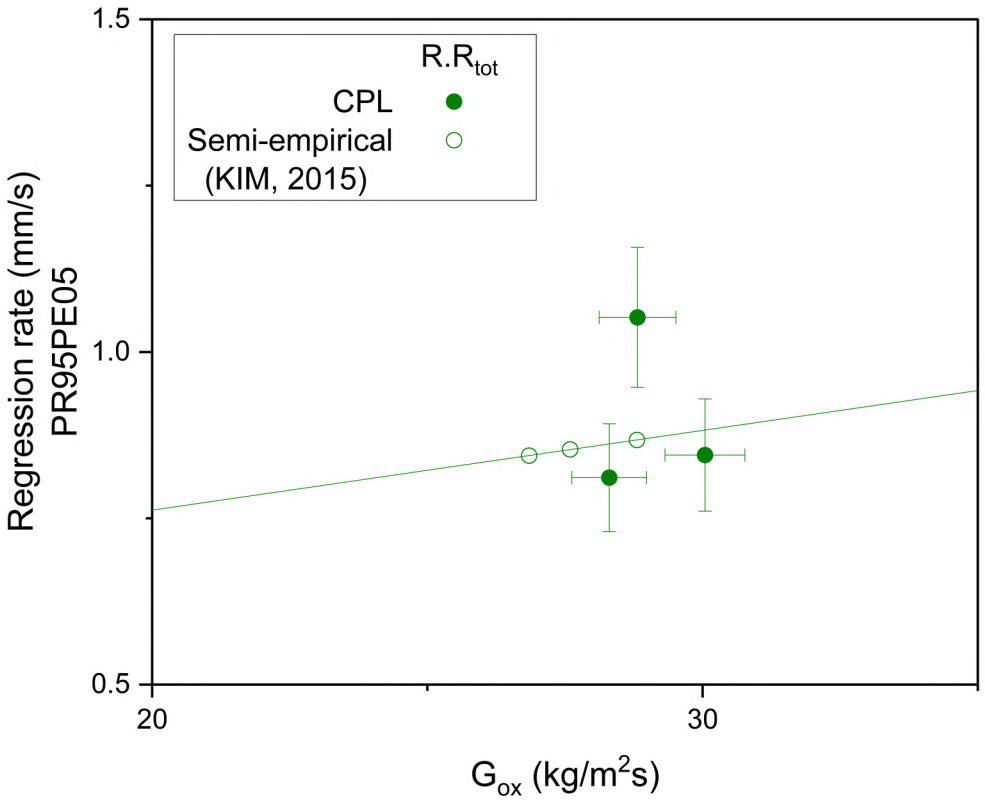

Figura 27 – Regression rate comparison with semi-empirical values for PR95PE05 fuel (Own authorship).

For the PR90PE10 blend, as can be seen in Figure 28, the liquid film regression rate decreased considerably when compared to the PR100 and PR95PE05 cases. As a result, the difference between the vaporization plus entrainment component and the liquid film regression rate became smaller, indicating that the film entrainment process is significantly suppressed in this more viscous blend. Still, the total regression rate measured experimentally remained higher than the theoretical prediction, reinforcing the trend observed in the other fuel compositions.

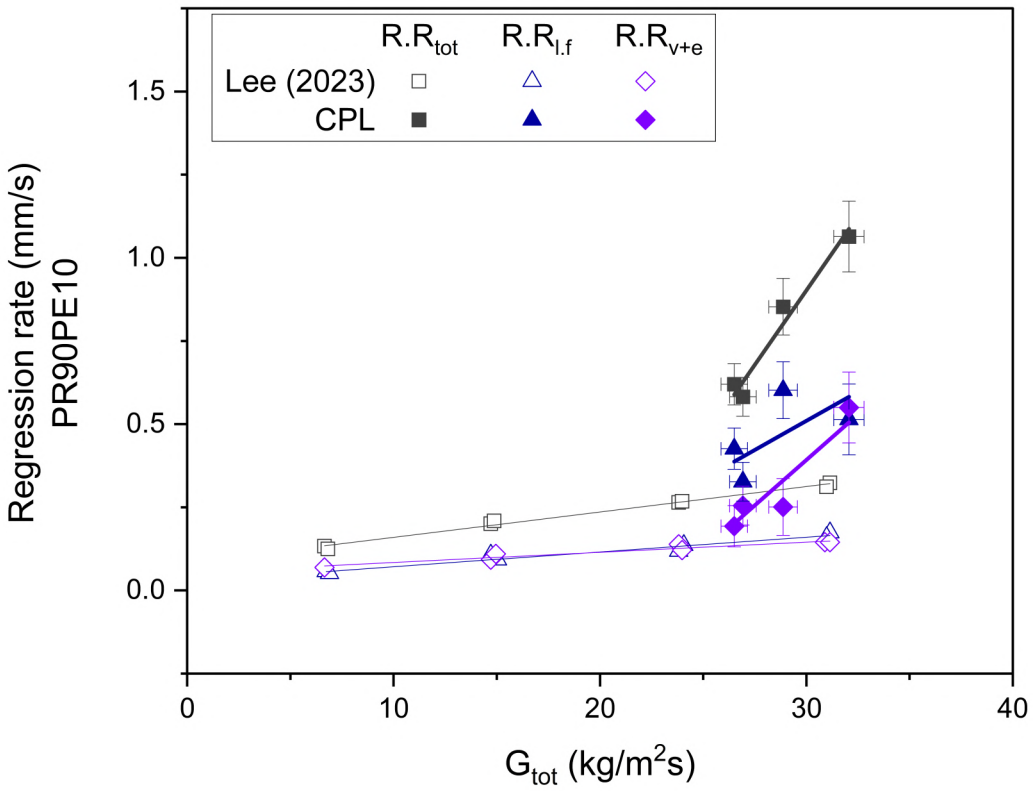

Figura 28 – Regression rates for PR90PE10 fuel (Own authorship).

Figure 29 presents the experimental regression rate data for the PR90PE10 fuel samples, plotted as a function of oxidizer mass flux (G_{ox}). The overall trend follows Equation 4.2.

$$\dot{r}_{tot} = 4.057 \times 10^{-7} \cdot G_{\text{ox}}^{4.392} \tag{4.2}$$

Although the first coefficient may seem small in magnitude, this is a direct consequence of the relatively high exponent (4.392) and the scale of the data involved. Since G_{ox} ranges between 25 and 29 g/cm²s and $\dot{r}_{\text{tot}}$ is on the order of 0.5 to 1.0 mm/s, the numerical compensation between these terms ensures a properly scaled regression curve. When trying to impose higher values for a, the result was a poor fit and loss of agreement with the experimental points.

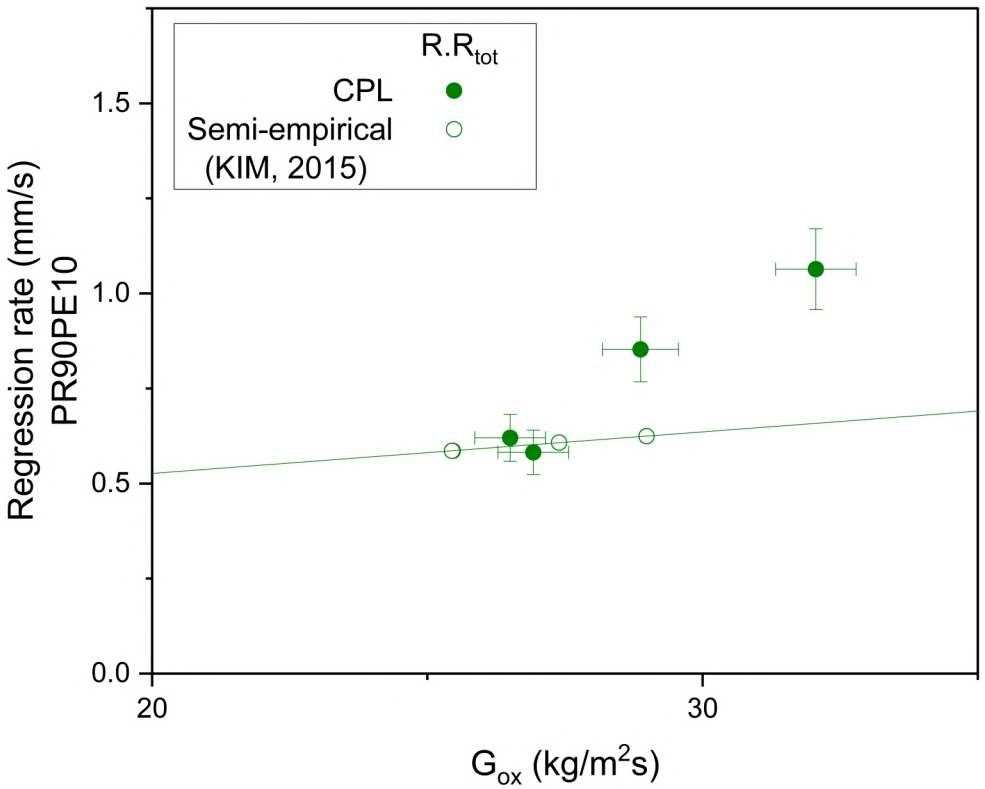

Figura 29 – Regression rate comparison with semi-empirical values for PR90PE10 fuel (Own authorship).

4.2 Discussion

In all three fuel compositions (PR100, PR95PE05, and PR90PE10), the total regression rates ($\dot{r}_{\text{tot}}$) measured at CPL were consistently higher than those reported by (LEE et al., 2023), even under similar G_{tot} conditions. This behavior is evident in Figures 24, 26, and 28, which present the regression rate components and their respective linear fittings.

Several factors may explain this behaviour:

- **Experimental conditions and repeatability:** Slight variations in the test conditions or ignition timing may have influenced the combustion environment.
- **Manual casting defects:** The use of manually fabricated samples introduced surface roughness and small defects, as can be seen in Appendix A, especially near the surface exposed to oxidizer flow. These defects likely intensified localized fuel melting.

- **Lower experimental density:** As discussed in Section 3.5, the actual density measured for each fuel sample was consistently lower than the theoretical value due to porosity and air bubbles. Since fuel density appears in the denominator of the regression rate formula, this underestimation increases $\dot{r}_{\text{tot}}$ for a given mass loss.
- **Burn time uncertainty:** Incomplete visual records of the flow meter led to estimations of burn duration, potentially introducing significant temporal error.
- **Fuel mass recovery:** Errors during the post-combustion collection of melted film and remaining fuel also contribute to uncertainty, as detailed in Chapter 3.5.
- **Effective burning area deviation:** As illustrated in the post-burn photos shown in Appendix B, much of the fuel grain burned beyond the theoretical surface area defined. Significant erosion was observed along the lateral edges and underside of the sample. As a result, the actual burning area A_w was greater than calculated, which can have caused an underestimation of the total burning surface and consequently inflated $\dot{r}_{\text{tot}}$.
- **Paraffin composition differences:** The paraffin wax used in this study (*SOLVEN 140 Wax*) is different from the Korean paraffin used by (LEE et al., 2023), which may have altered melting behavior, entrainment efficiency, or viscosity characteristics.

Despite these deviations in magnitude, the overall trends were preserved. In all cases, the total regression rate increases with G_{tot}, and the vaporization and entrainment contribution ($\dot{r}_{v+e}$) becomes increasingly dominant at higher mass flux values. This behavior reinforces the importance of entrainment mechanisms in hybrid fuels.

The curve fitting equations presented in this work are based on the current set of experimental data and should be interpreted as preliminary results. Due to the limited number of tests conducted, the regression models and their associated coefficients reflect only the available dataset and are not intended to represent a definitive or universal behavior. As further experiments are carried out and a broader range of operating conditions is explored, it is expected that the fitting curves will be refined, and the coefficients recalibrated to more accurately capture the underlying physical trends. Thus, the present models serve as a first approximation and a starting point for future validation and refinement.

To provide a comprehensive overview of the experimental results, Figure 30 compiles the total, liquid film, and vaporization and entrainment regression rates measured at CPL for all three fuel compositions. This comparison allows for a direct visualization of how the regression behavior evolves with increasing oxidizer mass flux and how the relative contribution of each regression mechanism varies across different paraffin–LDPE blends.

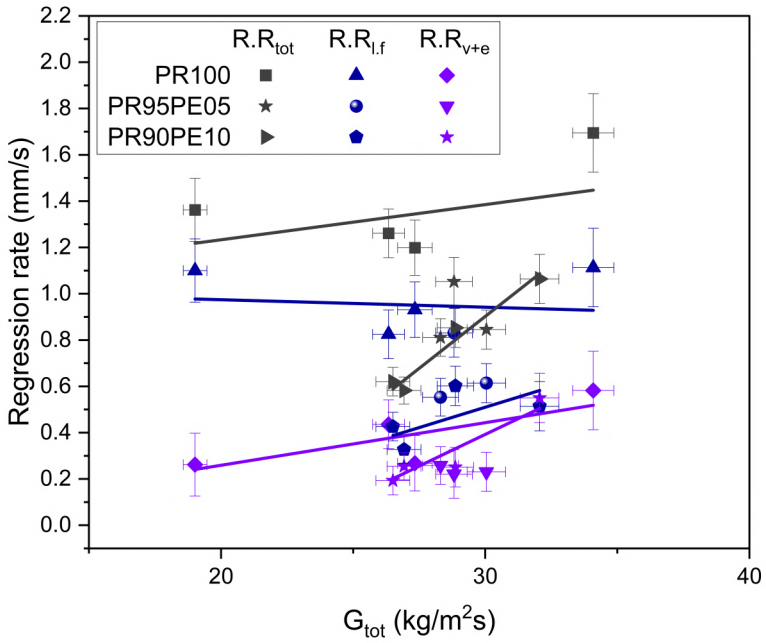

Figura 30 – Measured regression rates for all CPL fuels across varying G_{tot} (Own authorship).

4.3 Effect of LDPE Concentration and Combustion Efficiency Evaluation

The incorporation of LDPE into paraffin wax significantly influenced the combustion behavior and regression characteristics of the fuel samples. As observed in Figures 26 and 28, an increase in LDPE concentration correlates with a general reduction in the total regression rate, particularly for the PR90PE10 blend. This behavior is consistent with literature data, which suggest that excessive viscosity introduced by polymer additives may suppress the liquid film of melted fuel and the entrainment of liquid droplets due to limited surface mobility. In these conditions, the surface film becomes more stable.

From a performance standpoint, although the total regression rate is often used as a primary indicator of fuel behavior, combustion efficiency must also be considered. In the present open-burn slab burner configuration, it is not possible to quantify the characteristic velocity (c^*) or define combustion efficiency through conventional means. However, an alternative qualitative metric can be used: the convergence between the liquid film regression rate ($\dot{r}_{lf}$) and the vaporization + entrainment regression rate ($\dot{r}_{v+e}$). A smaller difference between these two rates indicates that less fuel is remaining in the molten film phase and more is being effectively vaporized and combusted.

Therefore, even if the total regression rate decreases with increased LDPE content,

a smaller gap between $\dot{r}_{lf}$ and $\dot{r}_{v+e}$ may suggest an improvement in combustion efficiency. This observation introduces a trade-off because the optimal formulation may not be the one with the highest $\dot{r}_{\text{tot}}$, but rather the one that balances the regression rate with minimal unused residue. This trade-off implies a need to optimize both entrainment effectiveness and thermal behavior, rather than maximizing any single metric in isolation.

5 Conclusion

This study experimentally investigated the regression behavior of paraffin-based hybrid fuels with varying concentrations of low-density polyethylene (LDPE) using a slab burner configuration. A total of 12 burn tests were conducted across three fuel compositions (PR100, PR95PE05, and PR90PE10), enabling the analysis of the effects of viscosity and fuel formulation on the overall combustion performance.

The oxidizer mass flow rate ($\dot{m}_{ox}$) ranged from approximately 18 g/s to 30 g/s, and the burn durations varied between 5 and 7 seconds depending on the test conditions. The resulting oxidizer mass fluxes (G_{ox}) spanned from approximately 17.6 kg/m$^2 \cdot$ s to 30.9 kg/m$^2 \cdot$ s. Total regression rates ($\dot{r}_{\text{tot}}$) ranged from 0.58 mm/s to 1.69 mm/s, while the liquid film regression rate ($\dot{r}_{lf}$) was significantly lower, particularly for higher-viscosity fuels, sometimes approaching 0.3 mm/s.

Experimental data consistently showed that the total regression rates observed at CPL were higher than those reported in the literature for equivalent G_{ox} values. This deviation is attributed to multiple factors, including imperfections in the fuel samples, the use of measured densities (which were lower than theoretical), and combustion extending beyond the theoretical burning area due to side and bottom burning. Notably, fuels with higher LDPE content (PR90PE10) exhibited reduced $\dot{r}_{\text{tot}}$, supporting the hypothesis that increased viscosity suppresses droplet entrainment and favors surface pooling.

To better capture the empirical behavior of hybrid fuel regression, nonlinear least squares fitting was applied to determine the parameters a and n in the relation:

$$\dot{r}_{\text{tot}} = a \cdot G^n$$

The resulting regression laws for two fuel compositions were:

$$\dot{r}_{\text{tot, PR100}} = 0.446 \cdot G_{\text{ox}}^{0.355}$$

$$\dot{r}_{\text{tot, PR90PE10}} = 4.057 \times 10^{-7} \cdot G_{\text{ox}}^{4.392}$$

These empirical equations are considered preliminary, as they were derived from a limited dataset. With fewer than 4–5 data points per fuel, the regression became highly sensitive to outliers. As such, these fits serve as first approximations of the regression behavior under the specific conditions tested. It is recommended that at least 20–25 experiments be conducted per formulation in future studies to enable robust determination of the coefficients and to refine the regression models.

Although the combustion chamber was open and did not allow for the calculation of conventional performance metrics such as characteristic velocity (c^*), the observed convergence between $\dot{r}_{lf}$ and $\dot{r}_{v+e}$ for certain formulations may suggest improved combustion efficiency. Future studies should aim to identify the optimal formulation where high total regression rates are maintained while minimizing the contribution from the liquid film, thereby enhancing the efficiency and controllability of the combustion process.

To reduce measurement uncertainty and improve the reliability of the experimental data, several improvements are proposed. One of the main sources of error in this study was the unintended burning of the bottom and lateral surfaces of the fuel grain, which caused the effective burning area to exceed the theoretical design. To address this, it is recommended that the fuel grain be bonded directly to the slab burner's base plate and that the grain width be increased to minimize side and bottom burning. Furthermore, integrating the ignition system into the test setup—thus avoiding manual ignition—would enhance repeatability and operational safety.

Referências

BERTOLDI, A. E. D. M. et al. Development and test of magnesium-based additive for hybrid rockets fuels. In: *15th International Conference on Space Operations*. Marseille: American Institute of Aeronautics and Astronautics, 2018. Citado 2 vezes nas páginas 5 e 28.

CAI, G. et al. Scale effect of fuel regression rate in hybrid rocket motor. *Aerospace Science and Technology*, v. 24, n. 1, p. 141–146, 2013. ISSN 1270-9638. VFE-2. Disponível em: <https://www.sciencedirect.com/science/article/pii/S1270963811001842>. Citado na página 32.

CANTWELL, B.; KARABEYOGLU, A.; ALTMAN, D. Recent advances in hybrid propulsion. *International Journal of Energetic Materials and Chemical Propulsion*, v. 4, p. 305–326, 2010. Disponível em: <https://doi.org/10.1615/IntJEnergeticMaterialsChemProp.v9.i4.20>. Citado na página 26.

COELHO, R. M. *Characterization of paraffin-LDPE blended fuels*. 2024. Trabalho de Conclusão de Curso, Universidade de Brasília. Disponível em: <https://bdm.unb.br/handle/10483/39893>. Citado 6 vezes nas páginas 7, 25, 26, 35, 41 e 49.

DEQUICK, B. *Two-phase flow numerical model of a paraffin-fueled hybrid rocket motor*. Dissertação (Master's thesis) — Université Libre de Bruxelles, Bruxelles, 2022. Citado 2 vezes nas páginas 5 e 20.

DUNN, C. et al. Spatially and temporally resolved regression rate measurements for the combustion of paraffin wax for hybrid rocket motor applications. *Aerospace Science and Technology*, v. 72, p. 371–379, 2018. ISSN 1270-9638. Disponível em: <https://www.sciencedirect.com/science/article/pii/S1270963816311002>. Citado na página 32.

GALFETTI, L. et al. Experimental investigation of paraffin-based fuels for hybrid rocket propulsion. *Progress in Propulsion Physics*, v. 4, p. 59–74, 2013. Disponível em: <https://doi.org/10.1051/eucass/201304059>. Citado na página 32.

GELAIN, R. et al. Design and commissioning of the mouette hybrid rocket slab burner. *9th European Conference for Aeronautics and Space Sciences (EUCASS)*, 2022. Citado 3 vezes nas páginas 7, 29 e 30.

GUEDES, G. G. TCC, *Análise do filme líquido de combustíveis à base de parafina*. 2024. Trabalho de Conclusão de Curso (Graduação em Engenharia Aeroespacial) – Universidade de Brasília. Citado 2 vezes nas páginas 5 e 40.

HIRATA, Y. et al. Improvement of regression rate and combustion efficiency of high density polyethylene fuel and paraffin fuel of hybrid rockets with multi-section swirl injection method. *47th AIAA/ASME/SAE/ASEE Jt. Propuls. Conf. Exhib.*, 2011. Citado na página 32.

HUMBLE, G. N. H. R. W.; LARSON, W. J. *Space Propulsion Analysis and Design*. [S.l.]: McGraw Hill, 2007. Citado na página 19.

HUMBLE, R. W.; HENRY, G. N.; LARSON, W. J. *Space Propulsion Analysis and Design*. [S.l.]: Learning Solutions, 1995. 768 p. Citado 2 vezes nas páginas 20 e 21.

ISHIGURO, T. et al. A study on combustion efficiency of paraffin-based hybrid rockets. In: *45th AIAA/ASME/SAE/ASEE Joint Propulsion Conference and Exhibit*. [S.l.: s.n.], 2011. AIAA Paper 2011-5679. Citado na página 26.

JENS, E.; CANTWELL, B.; HUBBARD, G. Hybrid rocket propulsion systems for outer planet exploration missions. *IAA Acta Astronautica Journal*, Elsevier, 2016. Citado na página 14.

KARABEYOGLU, A. et al. Scale-up tests of high regression rate paraffin-based hybrid rocket fuels. *Journal of Propulsion and Power*, v. 20, n. 6, p. 1037–1045, 2004. Citado na página 32.

KARABEYOGLU, M. A. *Transient combustion in hybrid rockets*. Tese (Doutorado) — Stanford University, California, set. 1998. Citado na página 19.

KARABEYOGLU, M. A.; ALTMAN, D.; CANTWELL, B. J. Combustion of liquefying hybrid propellants: Part 1, general theory. *Journal of Propulsion and Power 2002*, 2002. Citado 2 vezes nas páginas 15 e 22.

KARABEYOGLU, M. A.; CANTWELL, B. J.; ALTMAN, D. Development and testing of paraffin-based hybrid rocket fuels. In: *37th AIAA/ASME/SAE/ASEE Joint Propulsion Conference and Exhibit*. [S.l.: s.n.], 2001. (AIAA Paper 2001-4503). Citado na página 24.

KARAKAS, H. et al. Influence of micro-aluminum addition to paraffin-based fuels on graphite nozzle erosion rate. *AIAA 2020-3752. AIAA Propulsion and Energy 2020 Forum*, 2020. Citado 2 vezes nas páginas 14 e 15.

KIM, S. et al. Evaluation of paraffin–polyethylene blends as novel solid fuel for hybrid rockets. *Journal of Propulsion and Power*, v. 31, n. 6, p. 1750–1760, 2015. Citado 8 vezes nas páginas 5, 7, 23, 24, 25, 26, 28 e 32.

KNUTH, W. et al. Solid-fuel regression rate behavior of vortex hybrid rocket engines. *J. Propul. Power*, v. 18, 2002. Citado na página 32.

KOBALD, M.; CIEZKI, H.; SCHLECHTRIEM, S. Optical investigation of the combustion process in paraffin-based hybrid rocket fuels. In: _____. *49th AIAA/ASME/SAE/ASEE Joint Propulsion Conference*. [s.n.]. Disponível em: <https://arc.aiaa.org/doi/abs/10.2514/6.2013-3894>. Citado 2 vezes nas páginas 5 e 28.

KUO, K. K.; CHIAVERINI, M. J. Review of solid-fuel regression rate behavior in classical and nonclassical hybrid rocket motors. In: CHIAVERINI, M. J.; KUO, K. K. (Ed.). *Fundamentals of Hybrid Rocket Combustion and Propulsion*. Reston, VA: AIAA, 2007. cap. 2, p. 37–126. Citado na página 21.

LECCESE, G.; CAVALLINI, E.; PIZZARELLI, M. State of art and current challenges of the paraffin-based hybrid rocket technology. *AIAA Propulsion and energy Forum*, 2019. Citado na página 25.

LEE, J. et al. Mass transfer due to liquid film of paraffin-based fuels for hybrid rocket engines. *10th European Conference for Aeronautics and Space Sciences (EUCASS)*, 2023. Citado 12 vezes nas páginas 5, 7, 15, 16, 29, 30, 38, 39, 44, 50, 55 e 56.

LESTRADE, J. Y.; ANTHOINE, J.; LAVERGNE, G. Liquefying fuel in hybrid propulsion: first step towards a 1d model. In: *4th European Conference for Aerospace Sciences*. [S.l.: s.n.], 2011. p. 1–8. Citado na página 27.

MAHOTTAMANANDA, S. N. et al. Beeswax–eva/activated-charcoal-based fuels for hybrid rockets: Thermal and ballistic evaluation. *Energies*, v. 15, n. 20, p. 7578, 2022. Disponível em: <https://doi.org/10.3390/en15207578>. Citado 2 vezes nas páginas 5 e 23.

MARXMAN, G. A.; WOOLDRIGE, C. E.; MUZZY, R. J. Fundamentals of hybrid boundary-layer combustion. In: WOLFHARD, H. G.; GLASSMAN, I.; GREEN, L. (Ed.). *Heterogeneous Combustion*. New York: Academic Press, 1964, (Progress in Astronautics and Aeronautics, v. 15). p. 485–522. Citado na página 24.

MUNDOGEO. *Innospace lança foguete e se torna a 1ª empresa privada a operar em Alcântara*. 2023. Accessed for reference and image. Disponível em: <https://mundogeo.com/2023/03/19/innospace-lanca-foguete-e-se-torna-a-1a-empresa-privada-a-operar-em-alcantara/>. Citado 2 vezes nas páginas 5 e 15.

NAKAGAWA, I.; HIKONE, S. Study on the regression rate of paraffin-based hybrid rocket fuels. *Journal of Propulsion and Power*, v. 27, n. 6, p. 1276–1279, 2011. Citado na página 26.

NASA. *Safety standard for oxygen and oxygen systems*. [S.l.]: NASA NSS 1740.15, 1996. 288 p. Citado na página 45.

NASA. *NASA System Safety Handbook*. [S.l.]: NASA/SP-2010-580, 2011. 102 p. Citado na página 44.

NASA. *13th Through 16th Centuries*. Unknown year. Figura 3. 241 x 173 pixels. Disponível em: <https://go.nasa.gov/3Lw1e2N>. Acesso em: 03 mai 2023. Citado 2 vezes nas páginas 5 e 18.

OISHI, T.; TAMARI, M.; SAKURAI, T. Experimental investigation of a swirling-oxidizer-flow-type hybrid rocket engine using low-melting-point thermoplastic fuel and oxygen. *Aerospace*, 2023. Citado na página 15.

OMEGA Engineering, Inc. *FTB790 Series Turbine Flowmeters User Manual*. [S.l.], 2018. Available from: <https://assets.omega.com/manuals/M4625.pdf>. Citado na página 37.

PALOU, A. et al. Characterization of the composition of paraffin waxes on industrial applications. *Energy & Fuels*, v. 28, n. 2, p. 956–963, 2014. Citado na página 25.

SHYNKARENKO, O.; GONTIJO, M. Development of a thrust control system for rocket engines. *71st International Astronautical Congress (IAC)*, 2020. Citado 8 vezes nas páginas 5, 7, 25, 34, 36, 37, 44 e 46.

SUTTON, G. P.; BIBLARZ, O. *Rocket Propulsion Elements*. [S.l.]: John Wiley Sons, Inc., Hoboken, New Jersey, 2017. 767 p. Citado 10 vezes nas páginas 5, 7, 14, 18, 19, 21, 22, 24, 31 e 32.

TURNS, S. R. *An introduction to combustion : concepts and applications*. 3th. ed. [S.l.]: McGraw-Hill, 2011. Citado na página 19.

VEALE, K. et al. A review of the performance and structural considerations of paraffin wax hybrid rocket fuels with additives. *Acta Astronautica*, v. 141, 10 2017. Citado 4 vezes nas páginas 5, 27, 30 e 31.

WRITERS, S. *SpaceShipTwo: Overview and Specifications*. 2013. Accessed for an image reference. Disponível em: <https://www.space.com/19021-spaceshiptwo.html>. Citado 2 vezes nas páginas 5 e 15.

ZILLIAC, G.; KARABEYOGLU, M. Hybrid rocket fuel regression rate data and modeling. In: _____. *42nd AIAA/ASME/SAE/ASEE Joint Propulsion Conference & Exhibit*. AIAA/ASME/SAE/ASEE Joint Propulsion Conference Exhibit., 2006. Disponível em: <https://arc.aiaa.org/doi/abs/10.2514/6.2006-4504>. Citado 2 vezes nas páginas 22 e 32.

ÇENGEL, Y. A. *Termodinâmica*. 7. ed. [S.l.]: McGraw Hill, 2013. 1-1018 p. Citado na página 20.

Apêndices

APÊNDICE A – Fuel Sample Details

Sample 12 – PR100

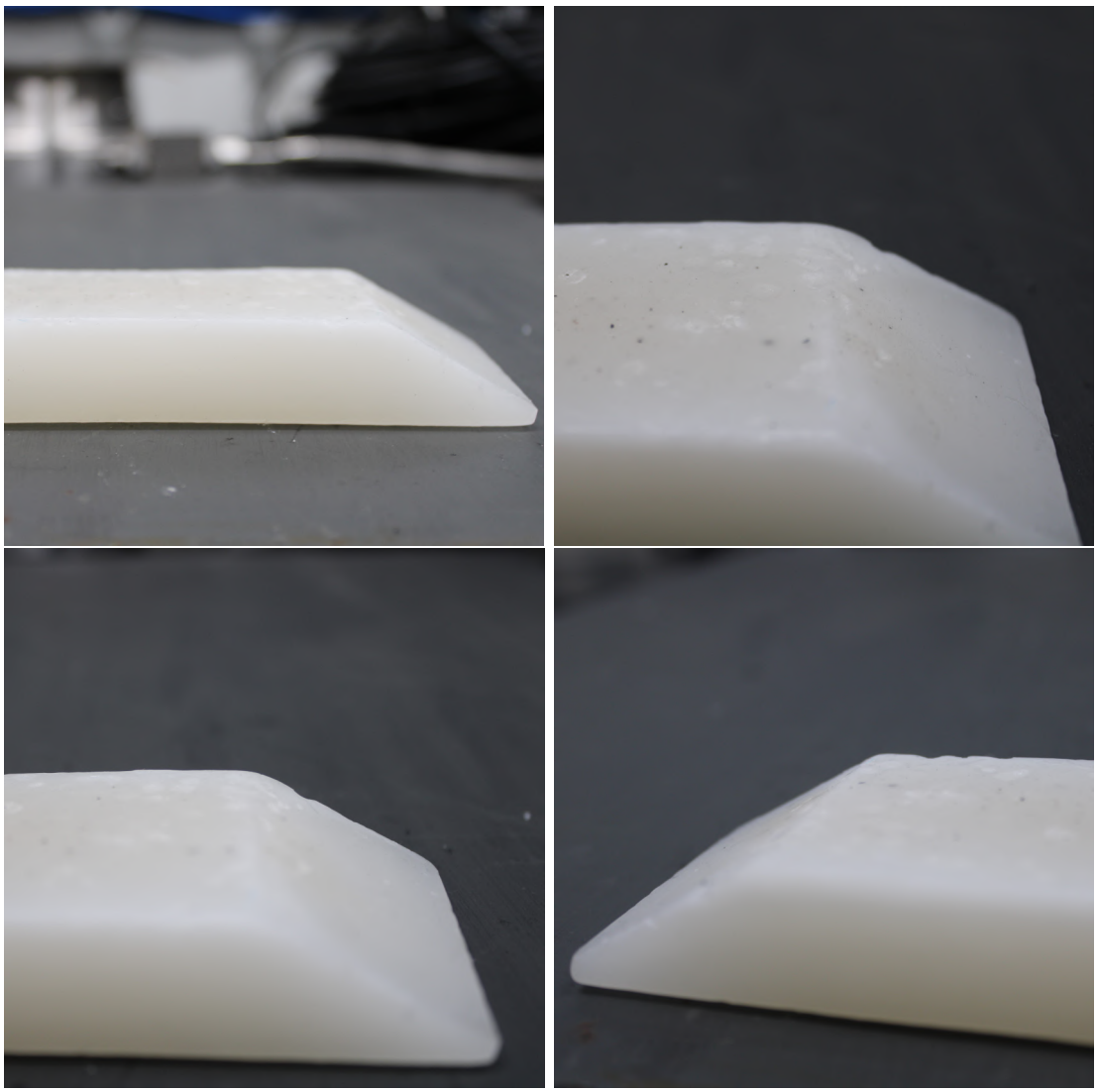

Figura 31 – Photographic documentation of Sample 12 (PR100).

Tabela 12 – Dimensional properties of Sample 12 – PR100.

Parameter	**Measured Value**	**Relative Error (%)**
Length (mm)	125.9	-2.70
Width (mm)	49.36	-1.28
Height (mm)	20.52	2.60
Mass (g)	104.6	-
Top section length (mm)	100.57	0.57
Length of inclined section (mm)	28.25	-
Inclined thickness (mm)	3.84	0.65
Burning area (m^2)	0.006358555	-

Sample 1 – PR100

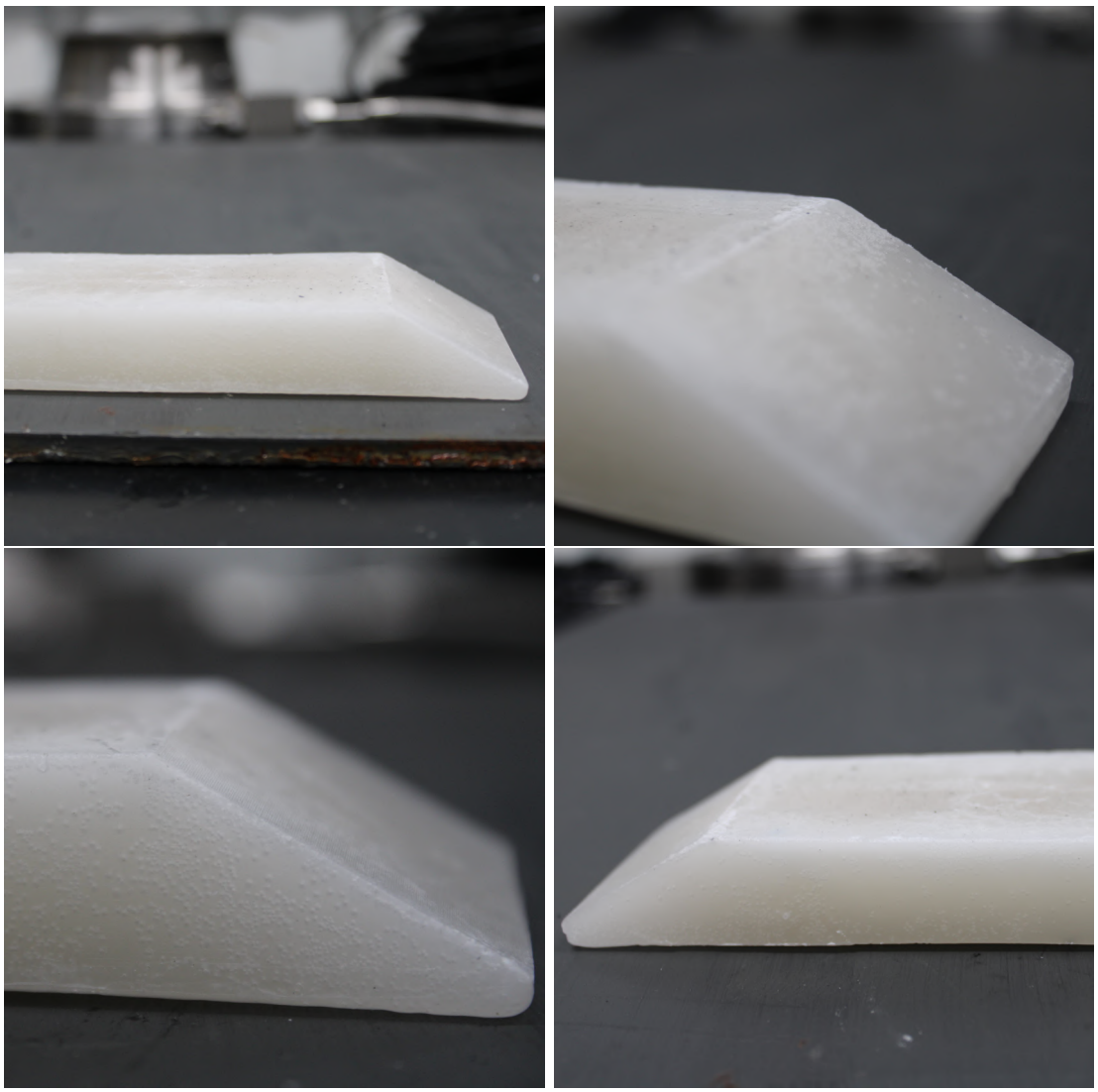

Figura 32 – Photographic documentation of Sample 1 (PR100).

Tabela 13 – Dimensional properties of Sample 1 – PR100.

Parameter	**Measured Value**	**Relative Error (%)**
Length (mm)	127.35	-1.58
Width (mm)	49.02	-1.96
Height (mm)	20.62	3.10
Mass (g)	101.8	-
Top section length (mm)	97.62	-2.38
Length of inclined section (mm)	32.61	-
Inclined thickness (mm)	4.73	1.34
Burning area (m^2)	0.006383875	-

Sample 2 – PR100

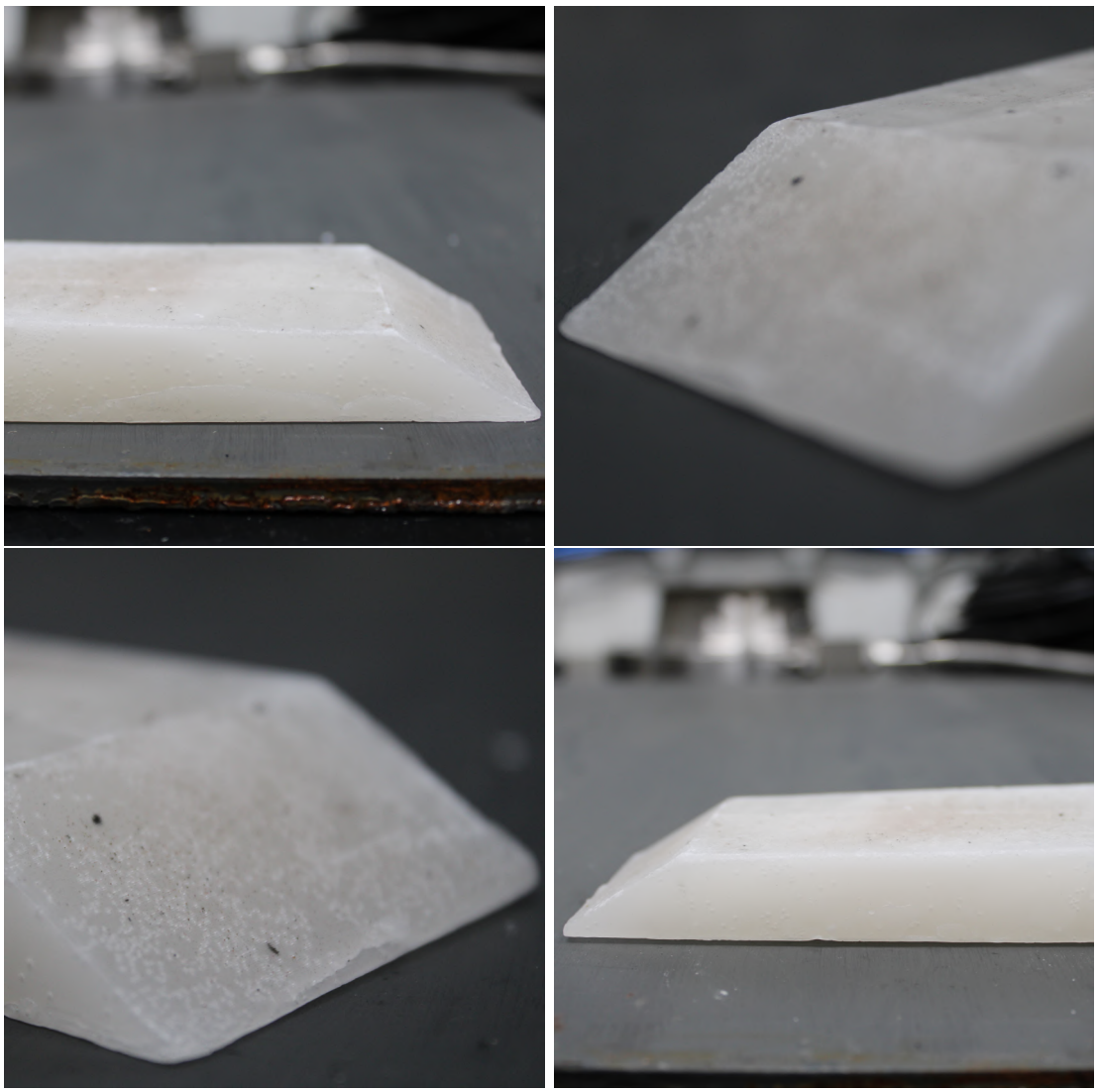

Figura 33 – Photographic documentation of Sample 2 (PR100).

Tabela 14 – Dimensional properties of Sample 2 – PR100.

Parameter	**Measured Value**	**Relative Error (%)**
Length (mm)	128.05	-1.04
Width (mm)	50.06	0.12
Height (mm)	20.15	0.75
Mass (g)	101.6	-
Top section length (mm)	101.51	1.51
Length of inclined section (mm)	30.26	-
Inclined thickness (mm)	8.77	4.46
Burning area (m^2)	0.006596406	-

Sample 3 – PR100

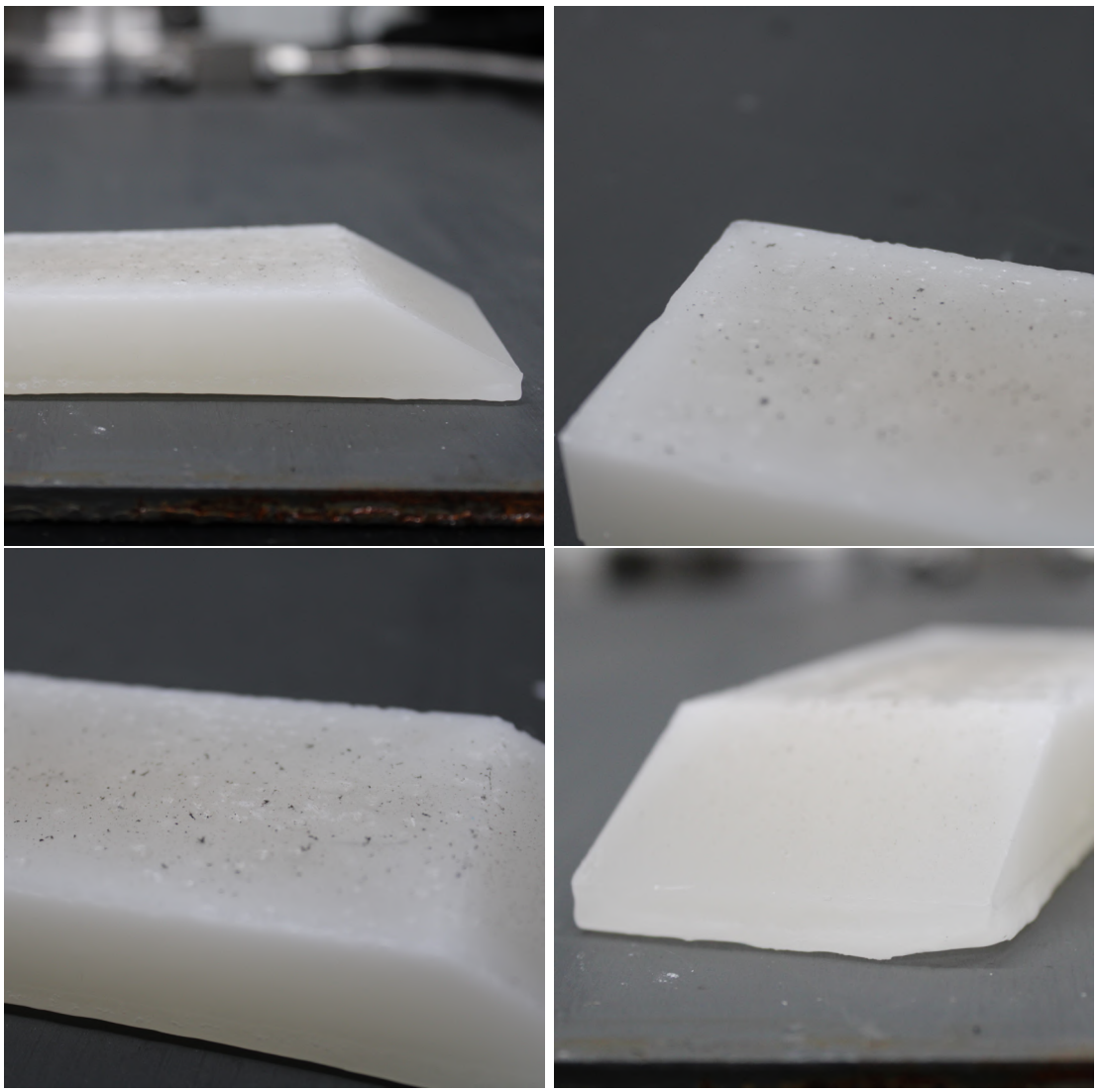

Figura 34 – Photographic documentation of Sample 3 (PR100).

Tabela 15 – Dimensional properties of Sample 3 – PR100.

Parameter	**Measured Value**	**Relative Error (%)**
Length (mm)	127.74	-1.28
Width (mm)	49.67	-0.66
Height (mm)	19.84	-0.80
Mass (g)	87.8	-
Top section length (mm)	97.60	-2.40
Length of inclined section (mm)	31.99	-
Inclined thickness (mm)	7.06	3.14
Burning area (m^2)	0.006436735	-

Sample 4 – PR95PE05

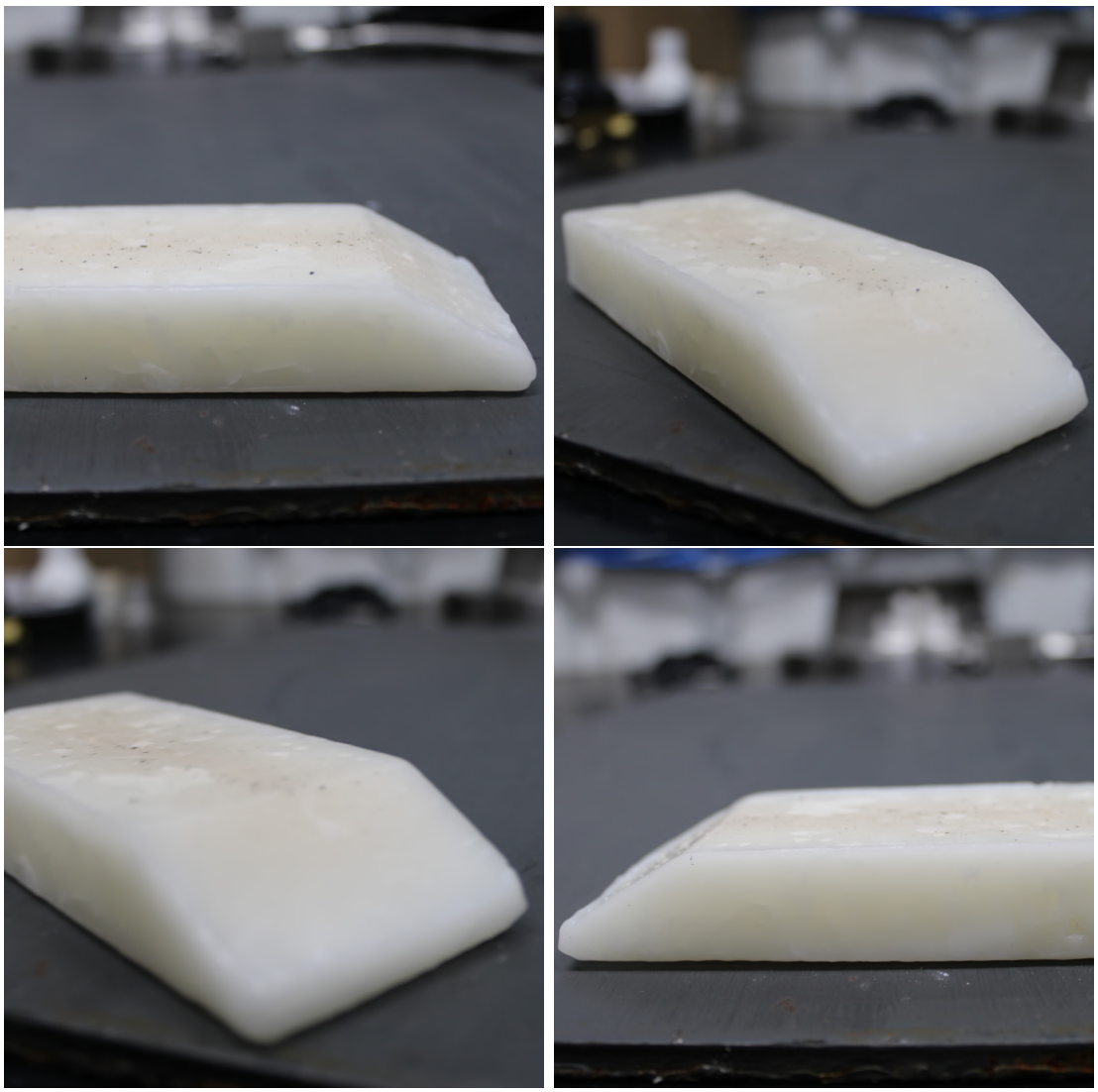

Figura 35 – Photographic documentation of Sample 4 (PR95PE05).

Tabela 16 – Dimensional properties of Sample 4 – PR95PE05.

Parameter	**Measured Value**	**Relative Error (%)**
Length (mm)	127.2	-1.70
Width (mm)	49.23	-1.54
Height (mm)	20.51	2.55
Mass (g)	105.2	-
Top section length (mm)	99.43	-0.57
Length of inclined section (mm)	29.73	-
Inclined thickness (mm)	9.54	5.05
Burning area (m^2)	0.006358547	-

Sample 5 – PR95PE05

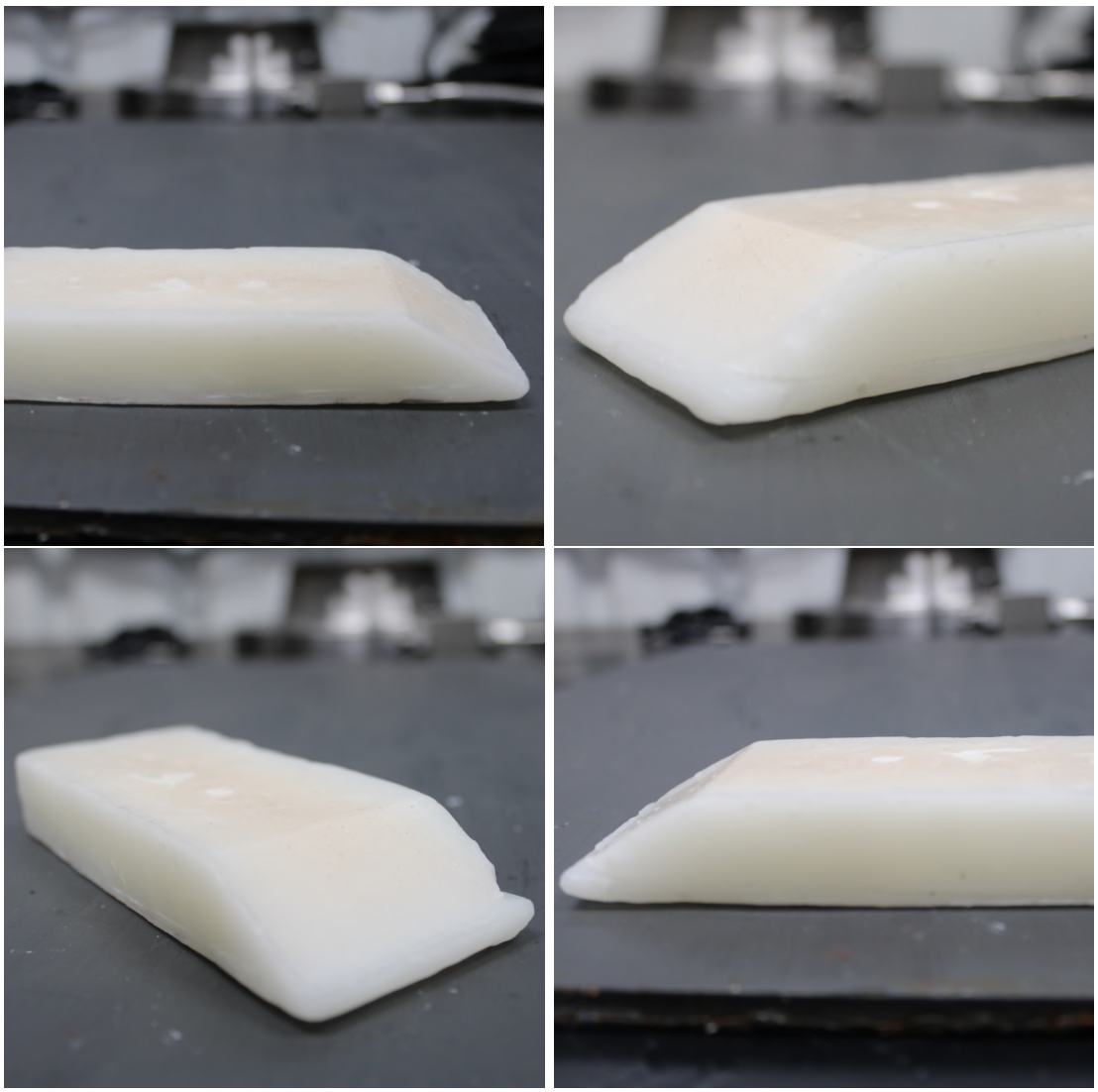

Figura 36 – Photographic documentation of Sample 5 (PR95PE05).

Tabela 17 – Dimensional properties of Sample 5 – PR95PE05.

Parameter	**Measured Value**	**Relative Error (%)**
Length (mm)	126.55	-2.20
Width (mm)	48.59	-2.82
Height (mm)	20.68	3.40
Mass (g)	101.1	-
Top section length (mm)	99.86	-0.14
Length of inclined section (mm)	31.48	-
Inclined thickness (mm)	5.74	2.12
Burning area (m^2)	0.006381811	-

Sample 6 – PR95PE05

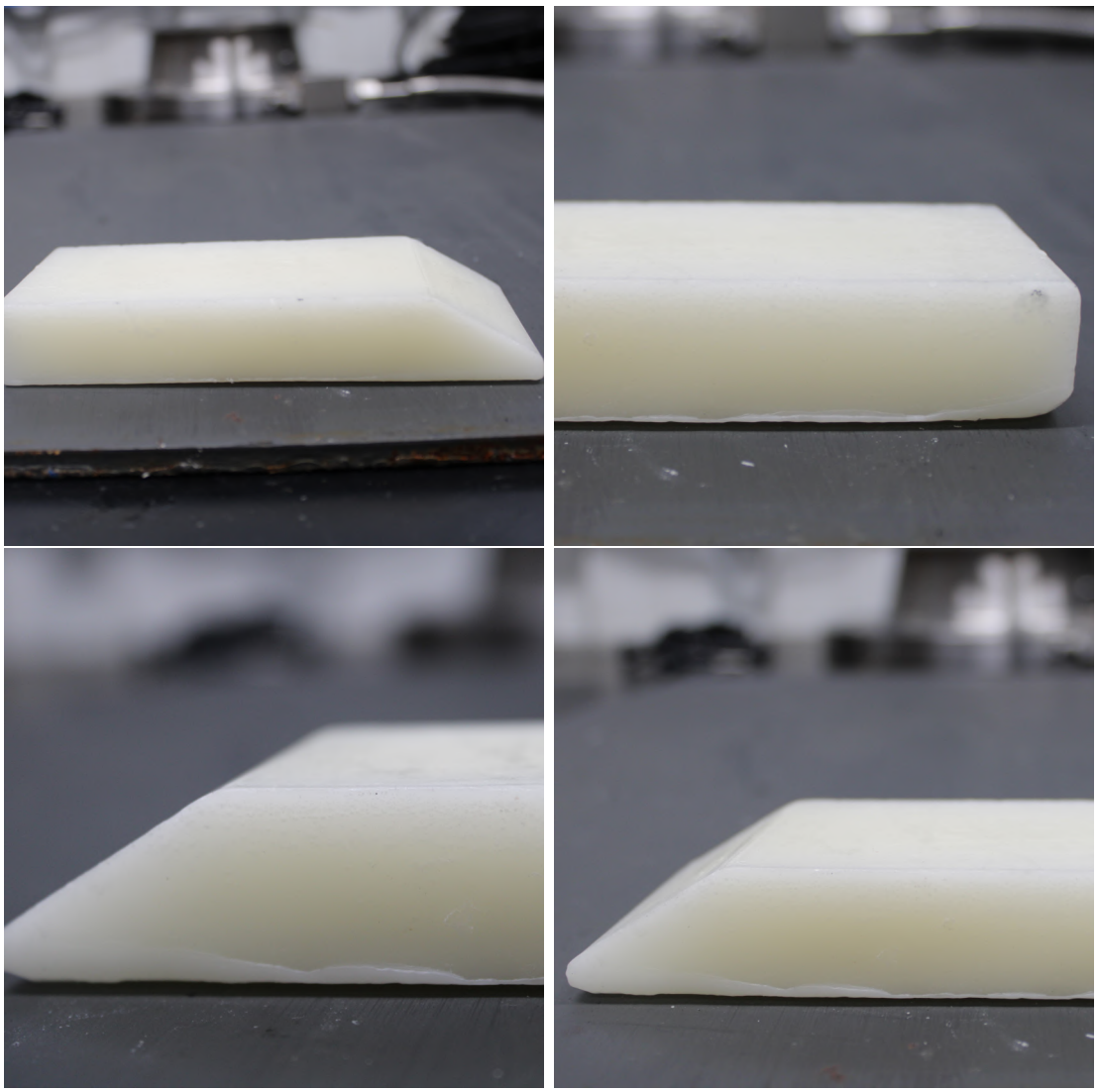

Figura 37 – Photographic documentation of Sample 6 (PR95PE05).

Tabela 18 – Dimensional properties of Sample 6 – PR95PE05.

Parameter	**Measured Value**	**Relative Error (%)**
Length (mm)	126.56	-2.19
Width (mm)	49.34	-1.32
Height (mm)	20.75	3.75
Mass (g)	108.1	-
Top section length (mm)	99.73	-0.27
Length of inclined section (mm)	31.17	-
Inclined thickness (mm)	7.51	3.49
Burning area (m^2)	0.006458606	-

Sample 7 – PR95PE05

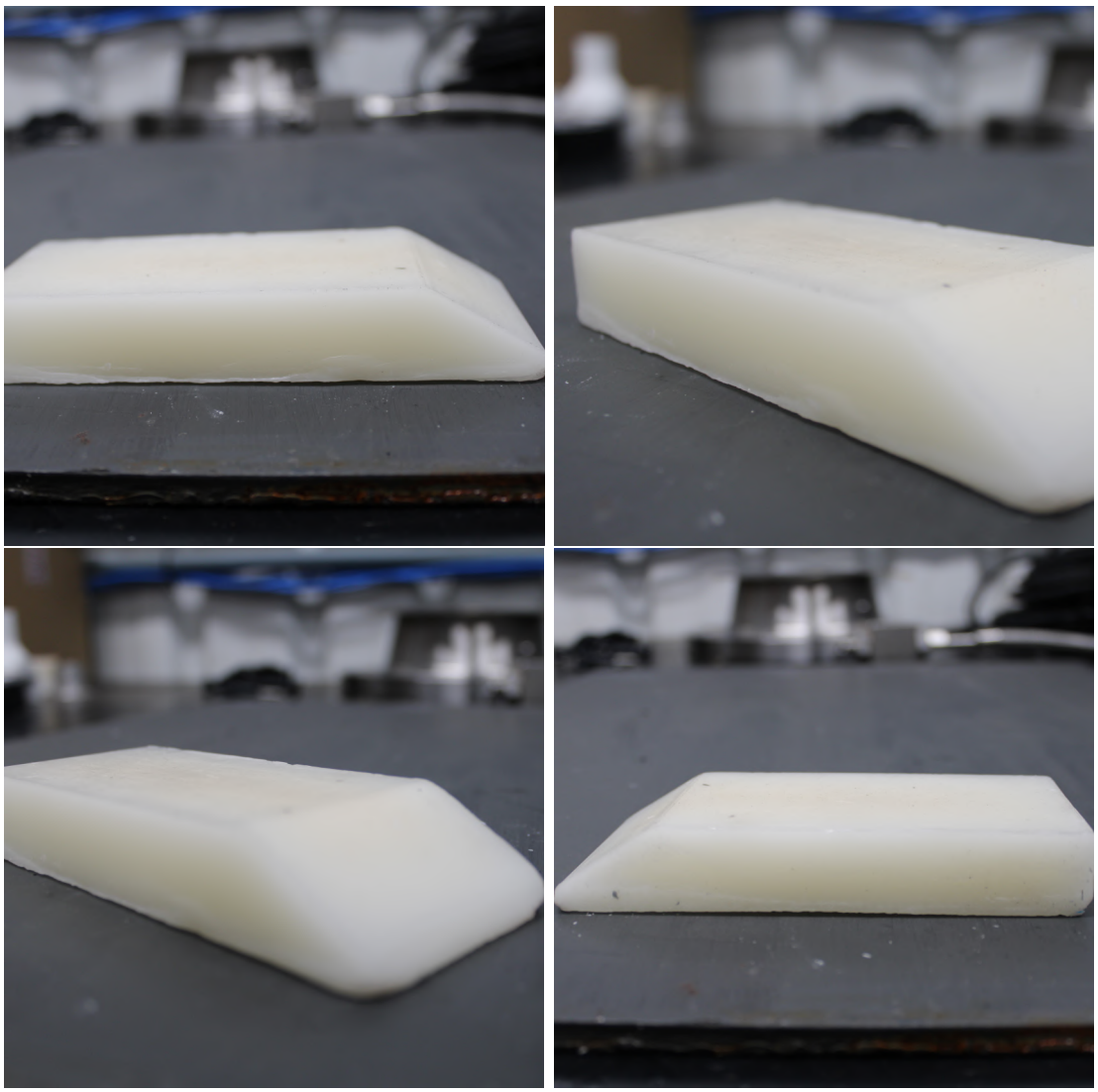

Figura 38 – Photographic documentation of Sample 7 (PR95PE05).

Tabela 19 – Dimensional properties of Sample 7 – PR95PE05.

Parameter	**Measured Value**	**Relative Error (%)**
Length (mm)	125.13	-3.30
Width (mm)	49.33	-1.34
Height (mm)	19.92	-0.40
Mass (g)	106.1	-
Top section length (mm)	99.79	-0.21
Length of inclined section (mm)	30	-
Inclined thickness (mm)	6.83	2.96
Burning area (m^2)	0.006402541	-

Sample 8 – PR90PE10

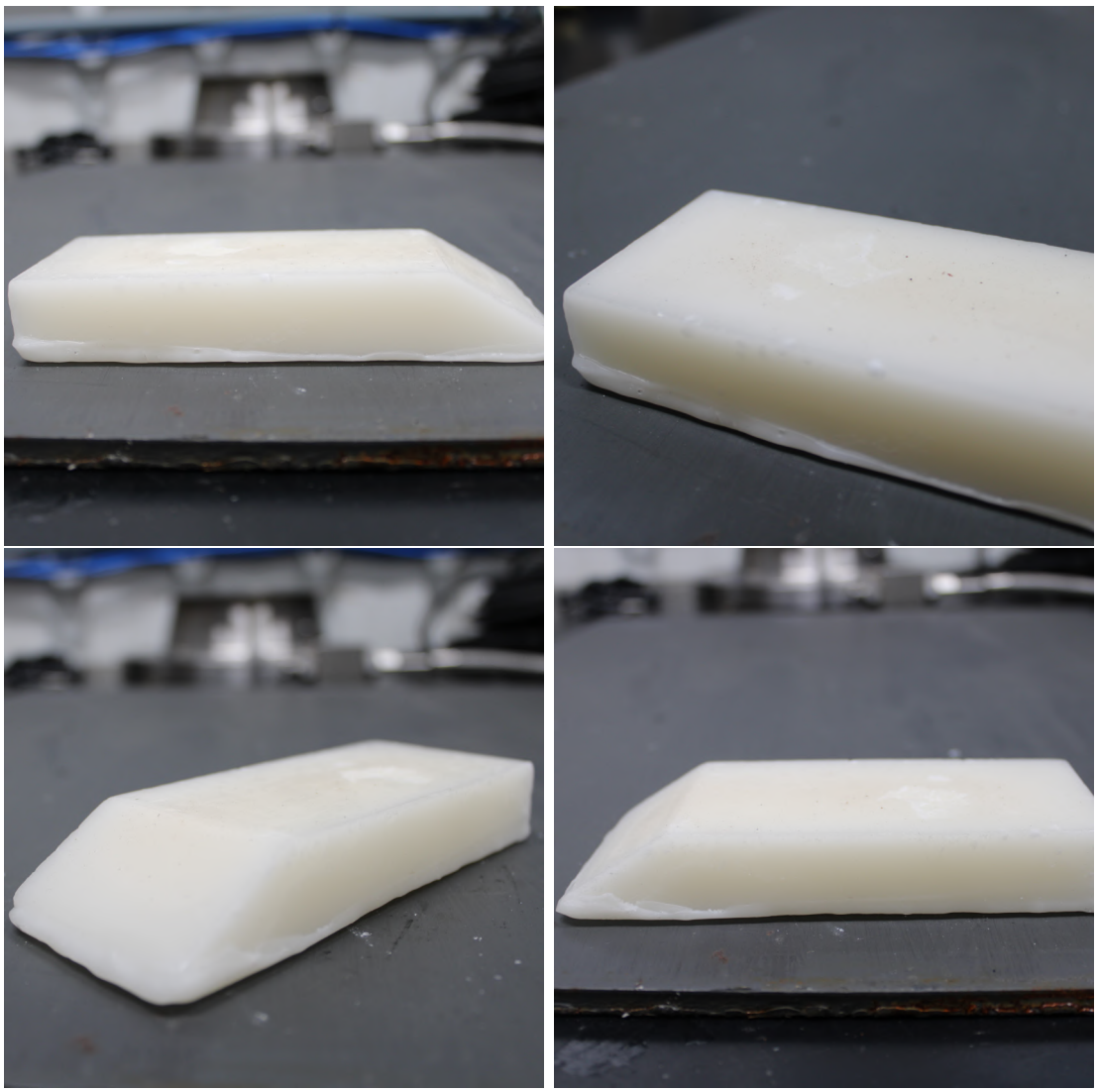

Figura 39 – Photographic documentation of Sample 8 (PR90PE10).

Tabela 20 – Dimensional properties of Sample 8 – PR90PE10.

Parameter	**Measured Value**	**Relative Error (%)**
Length (mm)	126.49	-2.25
Width (mm)	49.25	-1.5
Height (mm)	20.62	3.10
Mass (g)	107.7	-
Top section length (mm)	99.60	-0.40
Length of inclined section (mm)	29.29	-
Inclined thickness (mm)	5.92	2.26
Burning area (m^2)	0.006347833	-

Sample 9 – PR90PE10

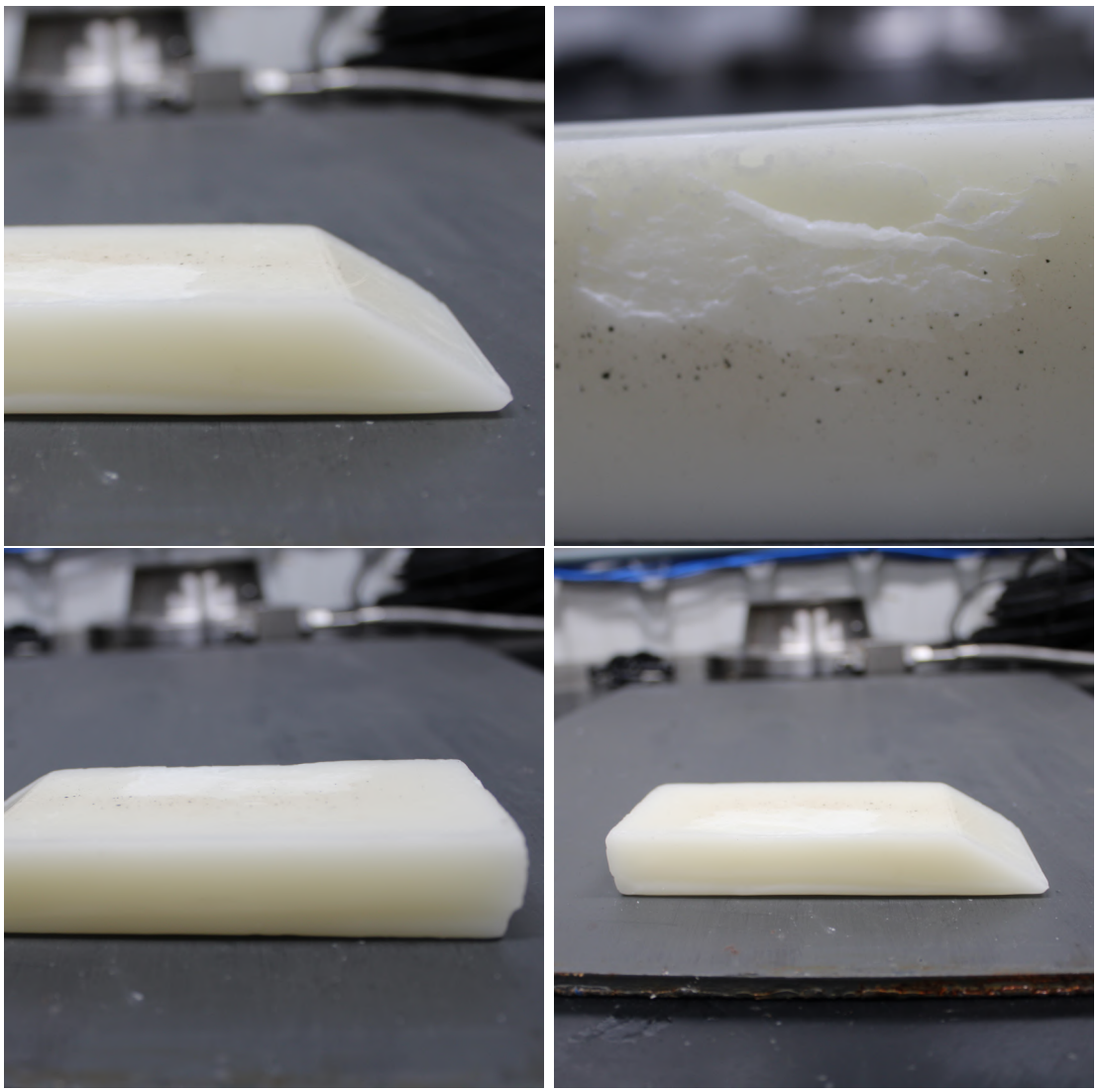

Figura 40 – Photographic documentation of Sample 9 (PR90PE10).

Tabela 21 – Dimensional properties of Sample 9 – PR90PE10.

Parameter	**Measured Value**	**Relative Error (%)**
Length (mm)	127.14	-1.75
Width (mm)	49.31	-1.38
Height (mm)	20.79	3.95
Mass (g)	101.6	-
Top section length (mm)	101.13	1.13
Length of inclined section (mm)	29.77	-
Inclined thickness (mm)	6.23	2.50
Burning area (m^2)	0.006454679	-

Sample 10 – PR90PE10

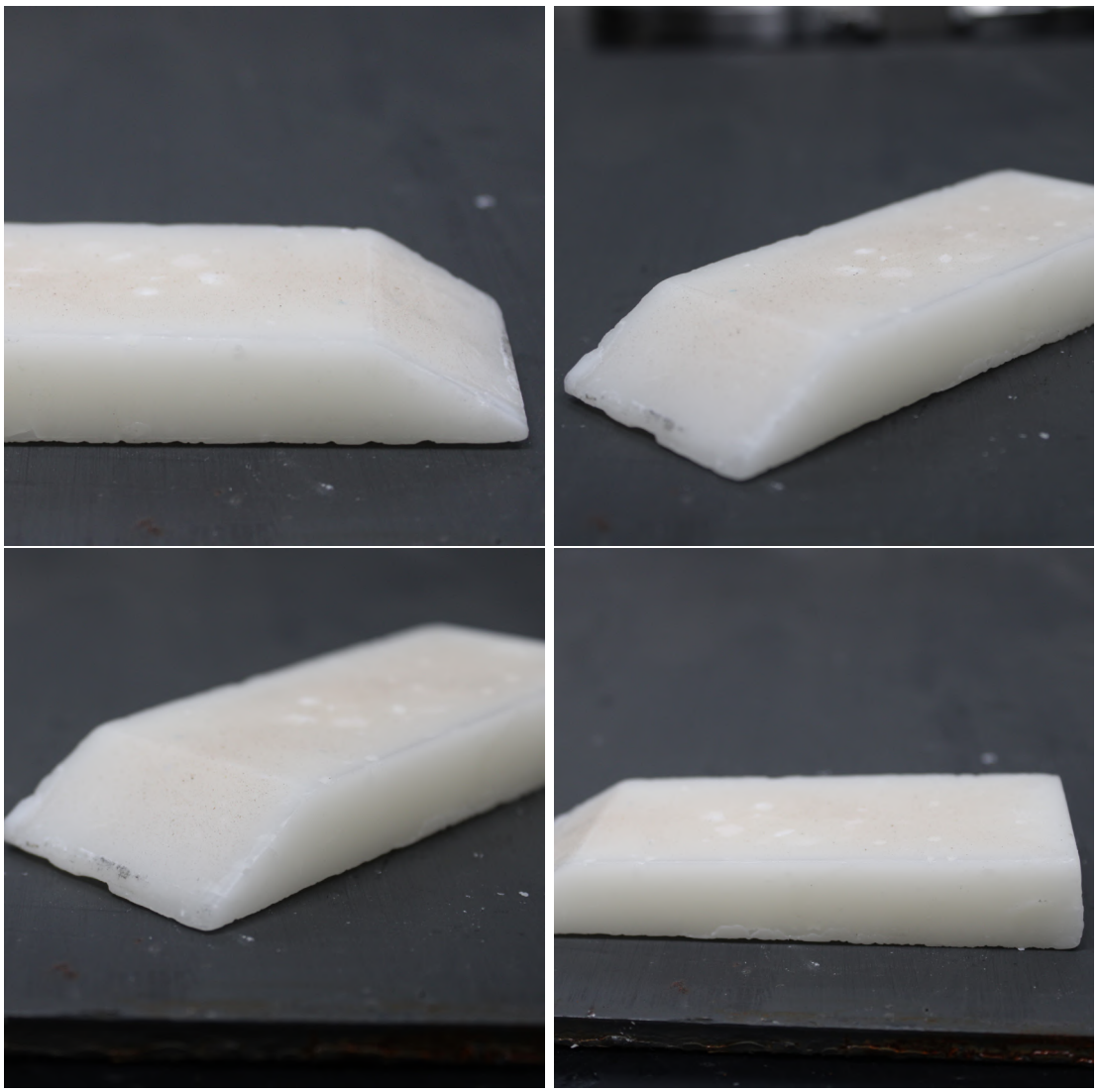

Figura 41 – Photographic documentation of Sample 10 (PR90PE10).

Tabela 22 – Dimensional properties of Sample 10 – PR90PE10.

Parameter	**Measured Value**	**Relative Error (%)**
Length (mm)	123.81	-4.32
Width (mm)	49.04	-1.92
Height (mm)	19.66	-1.70
Mass (g)	89.2	-
Top section length (mm)	100.86	0.86
Length of inclined section (mm)	28.31	-
Inclined thickness (mm)	3.39	0.30
Burning area (m^2)	0.006334497	-

Sample 11 – PR90PE10

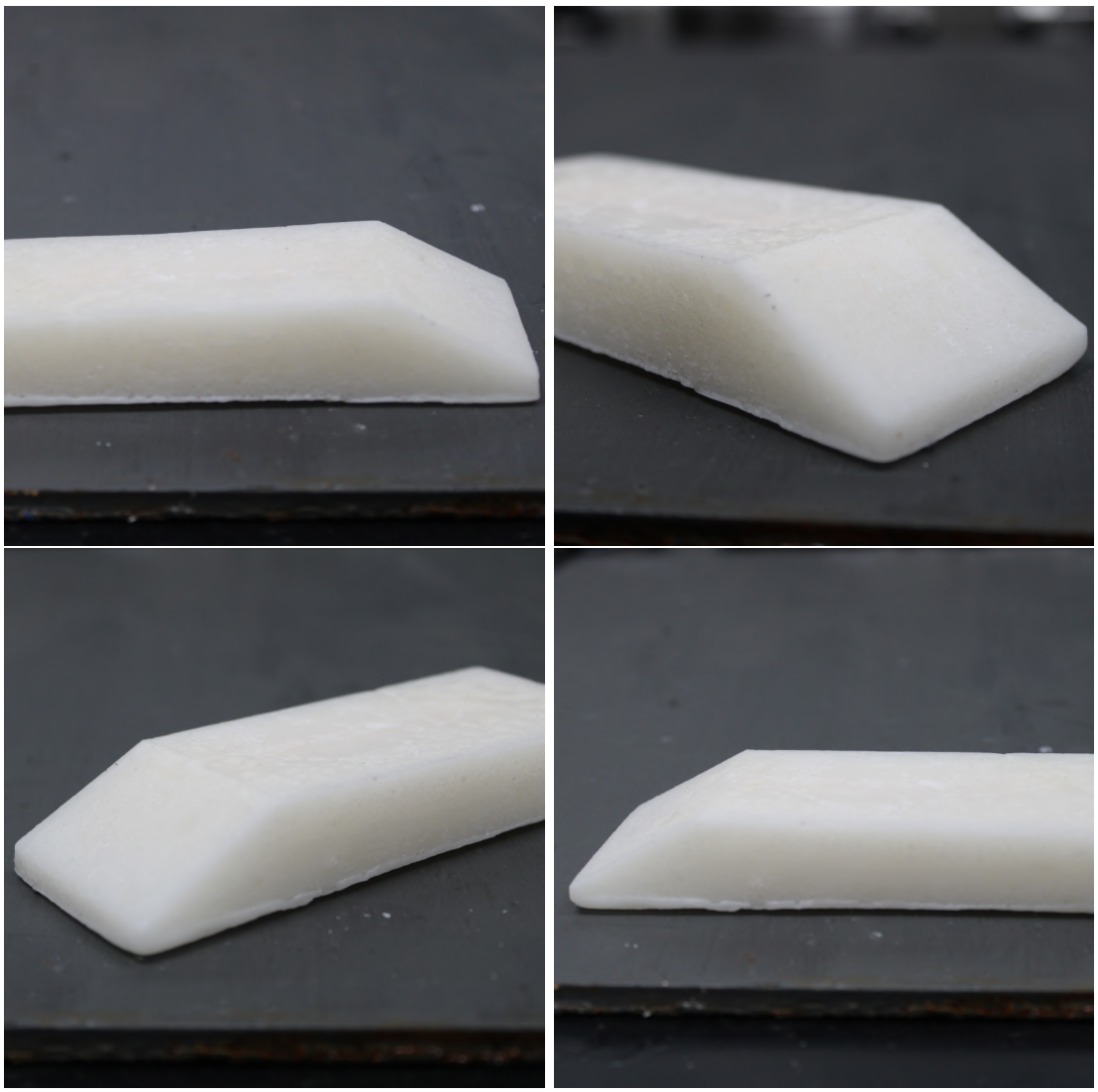

Figura 42 – Photographic documentation of Sample 11 (PR90PE10).

Tabela 23 – Dimensional properties of Sample 11 – PR90PE10.

Parameter	**Measured Value**	**Relative Error (%)**
Length (mm)	127.04	-1.82
Width (mm)	49.17	-1.66
Height (mm)	19.86	-0.70
Mass (g)	98.3	-
Top section length (mm)	97.90	-2.10
Length of inclined section (mm)	33.1	-
Inclined thickness (mm)	8.51	4.26
Burning area (m^2)	0.006441270	-

APÊNDICE B – Post-Combustion Fuel Samples

Sample 12 – PR100

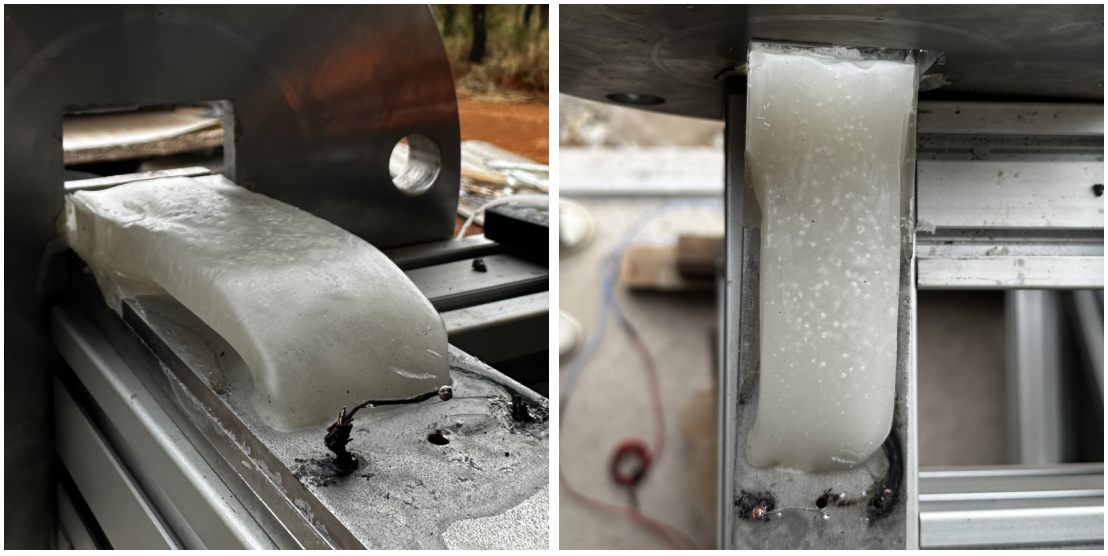

Figura 43 – Post-Combustion photographic documentation of Sample 12 (PR100).

Sample 1 – PR100

Figura 44 – Post-Combustion photographic documentation of Sample 1 (PR100).

Sample 2 – PR100

Figura 45 – Post-Combustion photographic documentation of Sample 2 (PR100).

Sample 3 – PR100

Figura 46 – Post-Combustion photographic documentation of Sample 3 (PR100).

Sample 4 – PR95PE05

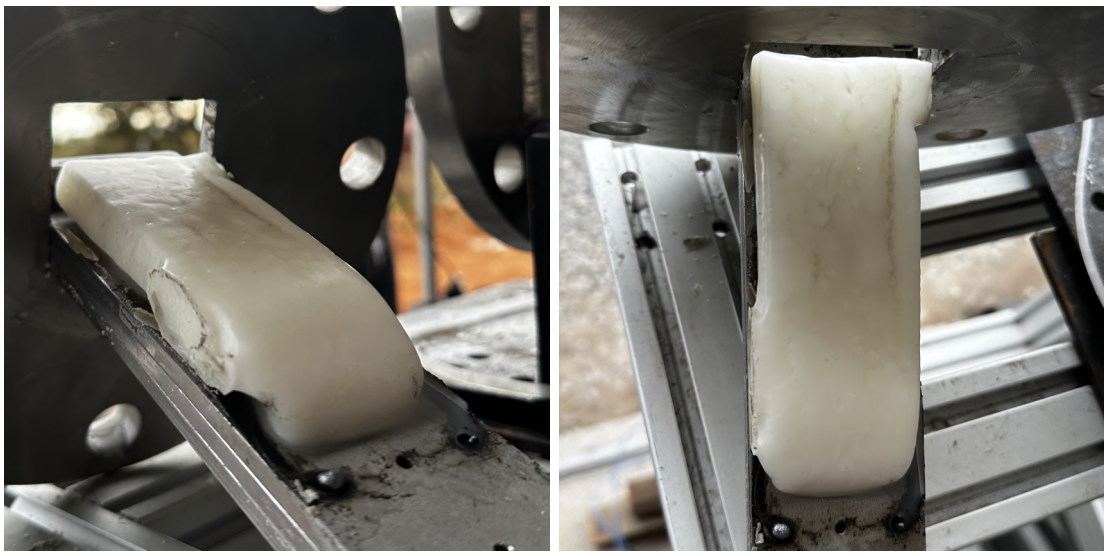

Figura 47 – Post-combustion photographic documentation of Sample 4 (PR95PE05).

Sample 8 – PR90PE10

Figura 48 – Post-combustion photographic documentation of Sample 8 (PR90PE10).

Sample 9 – PR90PE10

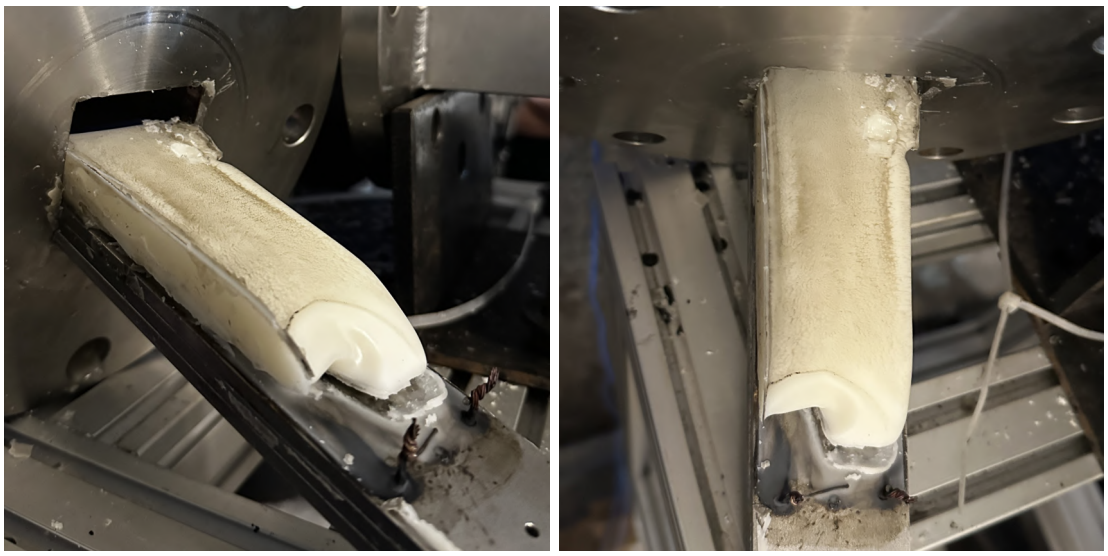

Figura 49 – Post-combustion photographic documentation of Sample 9 (PR90PE10).

Sample 10 – PR90PE10

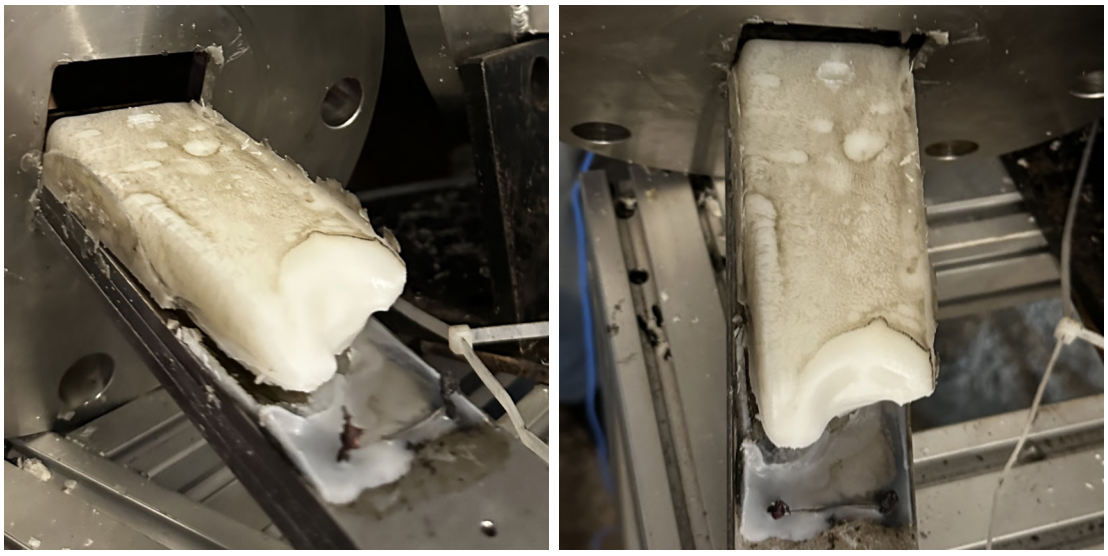

Figura 50 – Post-combustion photographic documentation of Sample 10 (PR90PE10).

Sample 11 – PR90PE10

Figura 51 – Post-combustion photographic documentation of Sample 11 (PR90PE10).

APÊNDICE C – Python Script for Nonlinear Curve Fitting

```python
import numpy as np
from scipy.optimize import curve_fit
import matplotlib.pyplot as plt

# Experimental data: oxidizer mass flux (Gox) and total regression rate (rtot)
Gox = np.array([26.341, 34.089, 27.337, 19.018]) # [kg/sm]
rtot = np.array([1.26093, 1.69479, 1.19895, 1.36216]) # [mm/s]

# Define the fitting model: r = a * G^n
def model(G, a, n):
    return a * G**n

# Perform nonlinear least squares fitting
params, covariance = curve_fit(model, Gox, rtot)

# Extract fitted coefficients
a, n = params
print(f"a = {a:.6f}")
print(f"n = {n:.6f}")

# Plotting the fitted curve (optional)
G_fit = np.linspace(min(Gox), max(Gox), 100)
r_fit = model(G_fit, a, n)

plt.scatter(Gox, rtot, label='Experimental data', color='blue')
plt.plot(G_fit, r_fit, label=f'Fit: r = {a:.4f}G^{n:.4f}', color='red')
plt.xlabel('$G_{ox}$ [kg/sm]')
plt.ylabel('Regression rate $\\dot{r}$ [mm/s]')
plt.legend()
plt.grid(True)
plt.title('Curve Fit of Regression Rate vs. $G_{tot}$')
plt.show()
```

Listing C.1 – Python script for nonlinear curve fitting using `scipy.optimize.curve_fit`